Polarization Diagnostics for Rubidium-80 in a Spin-Polarized Beta Decay Experiment

by

Daniel Grant Roberge

B.Sc., University of Victoria, 2004

A THESIS SUBMITTED IN PARTIAL FULFILMENT OF
THE REQUIREMENTS FOR THE DEGREE OF

Master of Science

in

The Faculty of Graduate Studies

(Physics)

The University Of British Columbia

September 2006

Abstract

The TRINAT group uses optical pumping to polarize atoms for precision spin-polarized beta decay experiments. This thesis describes two methods for determining the degree of polarization achieved in an experiment using ^{80}Rb: one method using atomic observables and one using nuclear observables. The atomic diagnostic uses a measurement of the excited state population over the duration of the optical pumping process to infer the polarization, while the nuclear diagnostic measures the beta decay asymmetry of the polarized atoms for a more direct polarization measurement.

The atomic diagnostic uses a simulation of the optical pumping process to calculate the excited state population over time as the atoms are optically pumped, along with the resulting polarization. The excited state population is in turn measured using a pulsed 355nm laser, with sufficient energy per photon to photoionize the excited state but not the ground state. Through variation of a 'polarization-spoiling' parameter the simulation can be fit to the data and a polarization value derived. The simulation is also applied to determine the laser power from a measurement of hyperfine pumping. The atomic diagnostic gives polarization values of $-0.887^{+0.031}_{-0.039}{}^{+0.022}_{-0.021}$ and $0.868^{+0.020}_{-0.010}{}^{+0.026}_{-0.030}$.

The nuclear diagnostic depends on a pair of back-to-back beta detectors placed at a 30-degree angle from the polarization axis. These detectors are used to measure the front-back asymmetry of the beta particles, which due to parity violation is proportional to the polarization of the decaying atoms. Due to systematic differences between the two detectors and their energy dependent corrections, the front-back asymmetry did not produce a useful polarization. Instead, the asymmetry in each detector between positive and negative polarization was used, which is also proportional to the polarization if the difference between the two polarizations is ignored. From this, one detector gives a polarization of (0.44 ± 0.01) and the other gives a polarization of (0.51 ± 0.01). These values are inconsistent both with each other and with the atomic result, but several differences between the sensitivity of the two methods may explain this discrepancy.

Table of Contents

List of Tables

List of Figures

Acknowledgements

No experimental science is ever a truly individual effort; not only do we, as Newton said, "see further" by "standing on the shoulders of giants" , but managing the complexity of a modern experiment alone is a difficult if not impossible task. I would like to take a moment to thank those people who have helped bring this thesis to fruition:

- My supervisor, John Behr, whose extensive knowledge of the physics and apparatus involved in this experiment was instrumental in this work. His willingness to talk about the experiment and help out at any time are greatly appreciated.
- My fellow grad student, Rob Pitcairn, who helped me remember the little things I forgot, tempered my caution with boldness, and was always around to join in blowing off steam.
- The rest of the TRINAT group: Matt Pearson, Gerald Gwinner, Conny Höhr, Alexandre Gorelov, Danny Ashery, Dan Melconian, and Erika Prime, and the undergraduate students who worked in the group during my time: Tam Nhan, Barbora Dej, Landon Halloran, and André Gaudin, for their assistance in tasks large and small.
- My thesis readers, Scott Oser and Kirk Madison, for their helpful feedback.

As always, I am grateful for the support of my friends and family, particularly when I've needed a break from working on my research.

To my parents, without whose support this work would not have been possible.

The laws of nature are constructed in such a way as to make the universe as interesting as possible.

-Freeman Dyson

Chapter 1

Introduction

Beta decay is a powerful tool for precision measurements of weak interaction physics. There is a strong theoretical understanding of beta decay, derived from its status as the first weak interaction process to be discovered and studied. This understanding, at the same time as it aids interpretation of beta decay experiments, makes beta decay measurements sensitive to small and heretofore unknown effects.

The TRINAT (TRIumf Neutral Atom Trap) apparatus at TRIUMF is designed for precision spin-polarized decay experiments, using radioactive atoms produced in the ISAC (Isotope Separator and ACcelerator) facility. TRINAT uses a magneto-optical trap (MOT) to confine the atoms within a detection chamber, and while so confined, the atoms can be manipulated. This thesis describes the process by which the atoms are polarized, and the measurements used to determine the degree of polarization attained in this process.

1.1 The TRINAT Apparatus

A MOT is a useful tool for precision experiments because it provides a well-localized collection of hundreds of thousands or millions of approximately stationary atoms in free space. When it is used to trap radioactive atoms, it allows us to study their decay from an accurately-known initial condition. While the MOT potential is deep enough to contain the initial radioactive atoms, it does not affect the transmuted decay product, which can escape freely. Having escaped the trap, the recoiling ion can then be detected. Through measurement of the recoil momentum and direction, many aspects of the decay can be reconstructed. A diagram of the TRINAT detection trap can be found in Figure 1.1.

The main mechanism of detection involves a static electric field of about 800 V/cm, combined with micro-channel plate (MCP) particle detectors. When a nucleus undergoes beta decay, its sudden recoil causes one or more electrons to 'shake off' the atom. Both the recoiling positive ions and the electrons are accelerated by the electric field, towards opposite ends of the chamber, where a position sensitive MCP is used to detect the ions, and a non-position sensitive MCP detects the electrons. The relative timing of these two detectors provides a time-of-flight measurement for the recoiling ion.

The detection chamber also contains several auxiliary detectors to measure the other

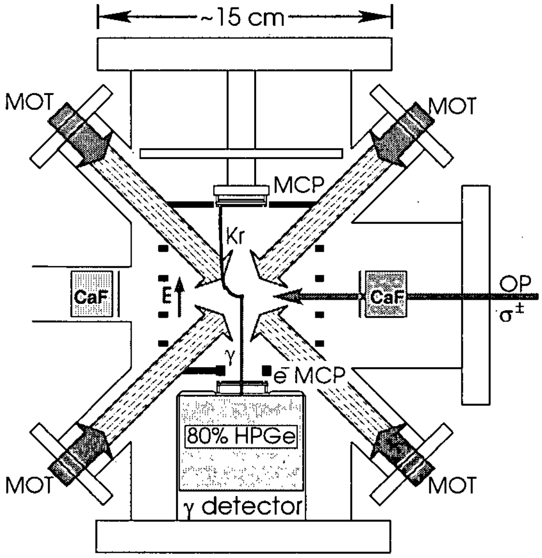

Figure 1.1: Diagram of the TRINAT detection trap

Push beam	Moves atoms into detection chamber
6 MOT trapping beams	Forces for Doppler cooling and Zeeman trapping
6 MOT repump beams	Prevents hyperfine pumping during MOT operation
Optical pumping beam	Polarizes atoms; includes pump and repump frequencies
Photoionization beam	Samples excited state population during optical pumping

Table 1.1: List of laser beams in the detection chamber

particles produced by the decay. Two CaF_2 'phoswich' detectors are situated opposite each other and pointed at the trap; these are designed to detect the positrons from β^+ decay for measurements of the beta asymmetry. The positrons are not significantly affected by the electric field as their high initial velocity allows them to rapidly escape its area of effect. A HPGe gamma-ray detector was placed behind the electron MCP to detect the gamma rays emitted when beta decay populates a nuclear excited state. In addition to these particle detectors, a computer-controlled video camera is used to view the trap size through detection of atomic fluorescence.

The apparatus pictured in Figure 1.1 contains the laser beams described in Table 1.1. The lasers are controlled with devices called acousto-optic modulators, or AOMs. An AOM shifts the frequency of light through interactions with sound waves in a crystal. An incident light beam is split into components each shifted by an integer multiple of the AOM's driving frequency; these components are each deflected proportional to their frequency shift. This 'steering' allows an AOM to be used as a switch; if the AOM is turned off the deflected beam vanishes. The frequency-shifted beam can be reflected back through the AOM to double the frequency shift; this 'double-pass' configuration has the advantage that the direction of the final beam is independent of the frequency shift.

1.2 Background for the ^{80}Rb experiment

A priori, there are five possible forms for the weak interaction vertex factor, corresponding to the five bilinear covariants: scalar, pseudoscalar, vector, axial vector, and tensor. In the experiments that led to the Standard Model theory of weak interactions, two of these appeared to be present: vector and axial vector, combined as $(V-A)$[16]. In nuclear physics, this is broken down into the 'Fermi' interaction and the 'Gamow-Teller' interaction, where the leptons produced from a Fermi decay have total angular momentum 0, and the leptons produced from a Gamow-Teller decay have total angular momentum 1[22].

Nevertheless, small contributions to the interaction with the other three forms have not been ruled out. An earlier TRINAT experiment[15] searched for scalar contributions to the beta decay of $^{38\mathrm{m}}$K. The superallowed $^{38\mathrm{m}}\mathrm{K} \rightarrow {}^{38}\mathrm{Ar}$ decay is a clean system, and is sensitive to scalar terms due to its pure Fermi nature. Fermi decays are sensitive to scalar and vector terms, while Gamow-Teller decays are sensitive to axial vector and tensor terms. Thus, to search for a possible tensor contribution, a pure Gamow-Teller decay is most useful.

Since the TRINAT apparatus can only trap alkali metal atoms, the field of isotopes available for study is relatively limited. Rubidium-80 was chosen for several reasons, the most important of which is its pure Gamow-Teller β^+ decay. Its hyperfine structure resembles that of ^{37}K, which was trapped in a previous TRINAT experiment, making a ^{80}Rb trap a straightforward adaptation of the preexisting apparatus. In particular, its ground state hyperfine splitting is comparable to that of ^{37}K. Also, the ISAC production rate for ^{80}Rb is relatively high, and the lifetime of ^{80}Rb is short enough to sustain a useful count rate with the expected trap population. The decay scheme of ^{80}Rb can be found in Figure 1.2. As can be seen in the figure, the vast majority of the decay strength (96%) is in two decays, from the 1^+ ground state of ^{80}Rb to either the 0^+ ground state or 2^+ first excited state of stable ^{80}Kr. All four of the decays shown in Figure 1.2 are pure Gamow-Teller decays, having a change in the nuclear spin of ±1. Thus, the decay of ^{80}Rb is sensitive only to the known, large axial vector component and the unknown, small tensor component.

In the Standard Model, the angular distribution of the positron produced in β^+ decay has, in the allowed approximation, a 'spin' asymmetry relative to the direction of the nuclear spin of the form[20]

$$A_\beta = -|M_{GT}|^2 K_1 + M_{GT} M_F K_2 \tag{1.1}$$

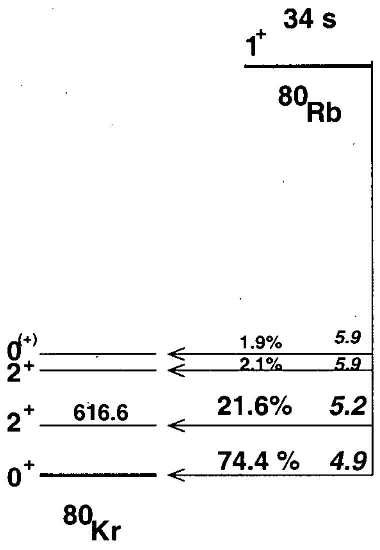

Figure 1.2: Simplified decay scheme of ^{80}Rb

Similarly, the spin asymmetry of the corresponding neutrino is given by

$$B_\nu = |M_{GT}|^2 K_1 + M_{GT} M_F K_3 \tag{1.2}$$

Here, K_1, K_2, and K_3 are combinations of the various weak coupling constants, M_{GT} is the Gamow-Teller matrix element, and M_F is the Fermi matrix element. In a pure Gamow-Teller decay, $M_F = 0$, and thus Equations 1.1 and 1.2 show that A_β and B_ν are equal and opposite. Since the spin asymmetry of the recoiling nucleus is given to first order as $A_R = 5/8(A_\beta + B_\nu)$, it is thus zero in the Standard Model for a pure Gamow-Teller decay. Hence, a nonzero recoil asymmetry can be interpreted as evidence of new physics, specifically tensor interactions.

1.3 Observables and Polarization

For a general beta decay, the angular distribution of the recoiling nuclei has the form[33]

$$W(\theta) = 1 + PA_R \cos\theta + CT \cos^2\theta \tag{1.3}$$

where P is the vector polarization of the nuclei in the trap, and T is their tensor alignment. (C is a constant of the decay depending on energies and coupling constants) Since this angular distribution is what the TRINAT apparatus samples, the quantity that can be measured is PA_R, not A_R by itself. Clearly, then, to accurately measure the recoil asymmetry A_R, the polarization must be known. The subject of this thesis is the measurement of the polarization P, while the measurement of PA_R is the subject of R. Pitcairn's M.Sc thesis[26].

Two main observables are available to characterize the polarization of the trap. The simpler observable is the angular distribution of the beta particles. The two back-to-back beta detectors measure this at a known angle to the polarization direction. As parity is maximally violated in beta decay, this angular distribution will be strongly forward peaked, and so the asymmetry between the two beta detectors will depend on the polarization. The interpretation of this data will be the subject of Part II.

A more powerful yet more complicated observable is the variation of the atomic excited state population over time. The process of optical pumping used to polarize the atoms excites more atoms when the polarization is low than when the polarization is high. Thus, as the atoms pump from fully unpolarized to fully polarized, the excited state population will drop.

The excited state population in the trap is sampled through photoionization by a 355 nm pulsed laser, which is only energetic enough to photoionize from the excited state of ^{80}Rb, and will not affect atoms in the ground state. The photoion laser produces 0.5 ns pulses at about 10 kHz; these pulses each photoionize a very small fraction of the atoms in the trap. These photoions are accelerated out of the trap and are detected in coincidence with the laser pulse, and then are counted over the duration of the optical pumping cycle to establish the variation of the population.

The relationship of this observable with the final polarization is complex. Part I will describe a simulation-based method of finding the polarization, as well as the theory behind both optical pumping and the basic operation of the MOT.

Part I

Atomic Physics

Chapter 2

Theory of Trapping and Pumping

The polarized ^{80}Rb decay experiment depends vitally on two atomic physics techniques: the magneto-optical trap (MOT) and optical pumping. The MOT is the fundamental basis of the TRINAT apparatus, while optical pumping allows for polarization of the atoms in the trap. This chapter will discuss the theoretical underpinnings of these processes, examining optical pumping more comprehensively as its details are vital to the goal of determining the atomic polarization.

2.1 Overview of MOT Physics

The magneto-optical trap is built using three pairs of counterpropagating laser beams and a magnetic quadrupole field. These two elements combine to both cool the atoms and trap them in a well-localized area, through a combination of the Doppler effect and the Zeeman effect. This combination provides a simple and robust device for containing atoms in free space.

A MOT uses an atomic transition called a 'cycling transition' to exert optical forces on the atom. In a cycling transition, the probability that the atom will return to its initial ground state after being excited is high, and so optical processes involving the absorption and emission of many photons can be made to proceed indefinitely as in the case of a two-level atom.[30] Since radiation pressure forces arise from the resonant or near-resonant scattering of many photons, they are most effective near a cycling transition.

Cycling transitions are most evident in atoms with simple internal structure, i.e. atoms with only a single valence electron. This chapter will assume that the atom under study is, like ^{80}Rb, an alkali metal satisfying this condition.

2.1.1 Doppler Cooling

The cooling action of the MOT is provided through a combination of detuned lasers and the Doppler effect. Consider a pair of counterpropagating laser beams detuned to the red of the atomic resonance by a frequency δ. Then, stationary atoms will not be resonant with the light, and thus will be affected symmetrically by the laser beams. If the atom is not stationary, but rather is moving with a speed v along the propagation direction of one of the lasers, both beams will appear Doppler shifted in the atom's reference frame[18]. The parallel beam will then appear to be detuned by $\delta + \frac{v\nu}{c}$ and the antiparallel beam will appear to be detuned by $\delta - \frac{v\nu}{c}$ (where ν is the frequency of the light). Thus, when the speed satisfies

$$\delta = \frac{v\nu}{c} \Rightarrow v = \frac{\delta c}{\nu} \tag{2.1}$$

the antiparallel beam is resonant, resulting in the absorption of photons from the antiparallel beam. Since the absorbed photons will all have momentum opposite that of the atom, and the spontaneously emitted photons will have randomly directed momentum, the result is a net optical force on the atom opposing its motion.

As the absorption cross-section decreases smoothly as the incident light moves away from resonance, the magnitude of the opposing force decreases smoothly as well. Thus, a velocity-sensitive damping force is generated along the axis of the two beams; the situation is analogous for an atom moving in the opposite direction due to the counterpropagating lasers. It is straightforward to generalize this using three orthogonal sets of counterpropagating lasers to generate a three-dimensional damping force, an effect referred to as 'optical molasses'.

2.1.2 Trapping Through the Zeeman Effect

Though optical molasses is useful for cooling, it does not provide a position-selective force, as is required for trapping. Ashkin and Gordon[5] showed that a system based only on radiation pressure cannot provide a position-selective force; only an optical gradient force can be position-selective. These optical gradient forces are weak, as they must induce a dipole moment in the atom rather than proceeding through some resonant process. Thus, very high laser intensities are required for significant confinement. However, we can circumvent this restriction because atoms have manipulable internal structure, rather than being simple dielectric particles as used by Ashkin and Gordon in their derivation.

In particular, atomic transitions can be shifted in energy through the application of a magnetic field, i.e. through the Zeeman effect. To provide the position sensitivity necessary for trapping, the magnetic field must vary in space. For the MOT, a quadrupole field is used, which has the crucial feature that it is zero at the centre and increases approximately linearly as one moves away from the zero.

Therefore, the Zeeman shift of the atomic levels also varies linearly with distance from the field zero. If counterpropagating beams of circularly polarized light are applied to the atom, the atomic transitions will move towards or away from the resonance as the atom moves, as shown in Figure 2.1.

If the circular polarization of the light beams is such that the beam from the negative-

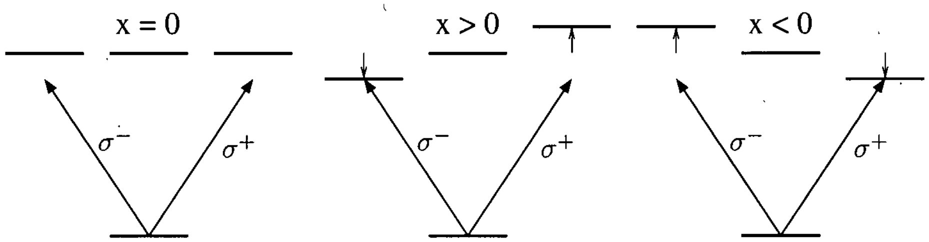

Figure 2.1: Diagram of Zeeman cooling

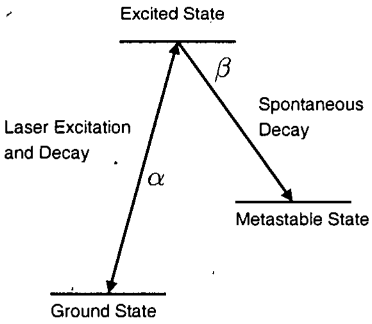

Figure 2.2: Diagram of optical pumping to metastable state

field direction has σ^- polarization, and the opposing beam has σ^+ polarization, then the atoms will experience a position-sensitive force directed towards the field zero. As a result, a three-dimensional potential, with the approximate form of a damped harmonic oscillator, is created with a potential minimum at the field zero. This occurs, for the most part, independently of the Doppler cooling effects, and the combination of these two effects is the magneto-optical trap.

2.2 Overview of Optical Pumping

In contrast to the cycling transitions used for trapping, optical pumping uses transitions that are deliberately one-way, intending to concentrate atomic populations in one part of the angular momentum manifold. Similar to the optical forces exploited by optical trapping, optical pumping depends on the interplay between consistent excitation and random decay to force the atoms into a particular internal state.

2.2.1 Basic Optical Pumping

Ignoring hyperfine structure for the moment, the conceptually simplest case of optical pumping involves a three-level atom with a metastable state, as shown in Figure 2.2. If the coupling between the ground state and the metastable state is weak or nonexistent, we cannot directly excite atoms from the ground state to the metastable state. Rather, an indirect route must be taken.

Given the presence of an excited state that couples to both the ground state and the metastable state, it can be used to optically pump from the ground state to the metastable state. If we denote the populations of the ground, excited, and metastable states as a, b, and c, respectively, with stimulated transition rate α and spontaneous decay rate β, we can write the following equations to describe the population changes:

$$\begin{aligned} \dot{a} &= -\alpha a + (\alpha + \beta) b \\ \dot{b} &= \alpha a - (\alpha + 2\beta) b \\ \dot{c} &= \beta b \end{aligned} \tag{2.2}$$

Here, we assume that the decay rate of the metastable state is negligible and that the spontaneous decay rates from the excited state to each of the other states are equal, for simplicity. The solution $c(t)$ of these differential equations is

$$c(t) = 1 - \frac{e^{-(\alpha+\beta)t}}{\omega}\left((\alpha+\beta)\cosh \omega t + \omega \sinh \omega t\right); \omega = \sqrt{\alpha^2 + \alpha\beta + \beta^2} \tag{2.3}$$

This function clearly goes to 1 as time goes to infinity, though the speed of optical pumping depends on the details of the rates.

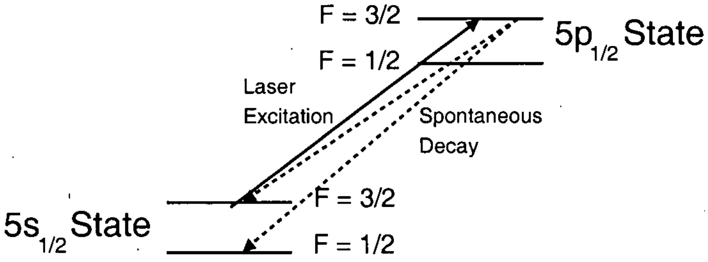

Figure 2.3: Diagram of hyperfine pumping in ^{80}Rb

If the ground and metastable states are replaced with the two hyperfine levels of the ground state (see Figure 2.3), the situation is analogous. If the laser is tuned well enough in frequency and has a narrow enough bandwidth, it will only excite from one of the hyperfine states, and by the same process as above will drive all of the population into the other hyperfine state. The speed of this pumping depends on the input laser intensity, and so this can be used as an *in situ* probe of the pumping laser power, as will be discussed in Chapter 4.

2.2.2 Circularly Polarized Optical Pumping

The case of optical pumping with circularly polarized beams is more complicated, as the full hyperfine structure of the atom must be taken into account. The ultimate goal of circularly polarized optical pumping is to add angular momentum to the atom until it reaches the state of maximum (or minimum) m_F, the 'fully-stretched' state. In the fully-stretched state, both m_J and m_I are also maximum, so both the electron and the nucleus are fully polarized.

Optical pumping with circularly polarized light differs from other cases of optical pumping in that a circularly polarized light beam has a definite angular momentum sign and thus only excites atomic transitions with a certain δm_F. Since spontaneous emission remains an unpolarized process, this has the net effect of adding angular momentum to the atom in the same way as radiation pressure forces add net linear momentum to the atom. A diagram of the intended process can be found in Figure 2.4.

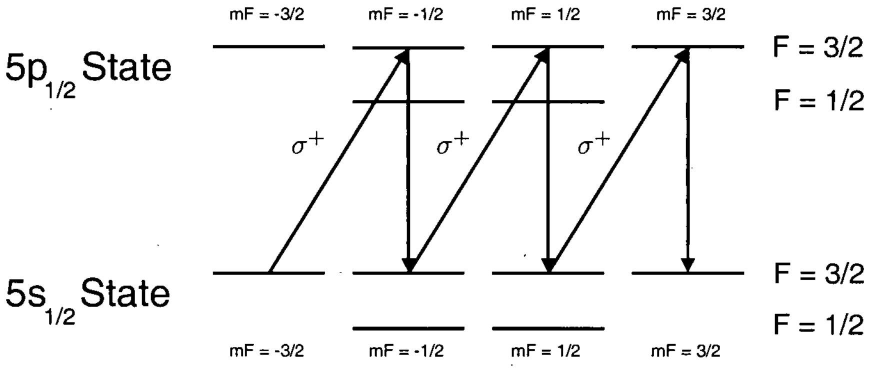

Figure 2.4: Optical pumping with circularly polarized light

The presence of two hyperfine levels in the ground state adds additional complications. The $F = 1/2$ sublevel cannot achieve full polarization, which requires $m_F = \pm 3/2$, so spontaneous decay to that sublevel impedes the optical pumping process. Since the pumping laser can only excite from one of the hyperfine sublevels, a second laser beam is necessary to 'rescue' those atoms that enter the $F = 1/2$ sublevel. This 'repump' laser should have the same circular polarization as the main pumping beam to maintain optimal efficiency of the pumping process. If the repump laser were not used, the hyperfine pumping effect described in the previous section would rapidly transfer most of the population into the $F = 1/2$ ground state, spoiling the intended polarization.

The differential equations that describe this process, ignoring both coherent effects and

AC Stark shifts, are the *rate equations*,

$$\frac{dN_{Gi}}{dt} = \sum_j \left(-R_{ij}N_{Gi} + R_{ji}N_{Ej} + \gamma_{ji}N_{Ej}\right) \tag{2.4}$$

$$\frac{dN_{Ej}}{dt} = \sum_i \left(R_{ij}N_{Gi} - R_{ji}N_{Ej} - \gamma_{ji}N_{Ej}\right) \tag{2.5}$$

In these equations, the index i varies over the set of ground states, and the index j covers the set of excited states. The rate of excitation, R_{ij} and the rate of stimulated emission R_{ji} are equal due to time reversal symmetry[10], while the spontaneous rate γ_{ji} only covers decay and not excitation. The form of these equations manifestly satisfies the condition

$$\sum_i \frac{dN_{Gi}}{dt} + \sum_j \frac{dN_{Ej}}{dt} = 0 \tag{2.6}$$

which ensures that the total population remains constant over time, i.e. it preserves unitarity.

2.2.3 Sufficiency of the Rate Equations

The full treatment of atom-laser interaction uses the optical Bloch equations[13], based on a density matrix formalism that naturally incorporates coherent couplings between the states. These coherent effects are ignored by Equations 2.4 and 2.5, whereas they can, in principle, occur in our system. The two laser beams used for pumping and repumping are derived from the same source and thus are coherent with each other, so analogous coherences could occur between atomic states perturbed by these lasers. In particular, the light field can mix states of different total angular momentum F and identical projection m_F. These coherently mixed states can have vanishing excitation rates in the same way as the fully-stretched state does, and so the system could appear to have a greater polarization than it actually has. The coherences become considerably more unstable when the degeneracy of the states in each hyperfine sublevel is broken using a magnetic field[7]; the TRINAT apparatus incorporates a constant axial magnetic field that satisfies this condition.

These 'coherent population trapping' states have been investigated by the TRINAT group in the past[17], and were found in the TRINAT system to require precise tuning of the frequency difference to match the ground state hyperfine Raman resonance. Detuning the lasers from this point destroyed the dark coherent state, restoring the semiclassical behaviour described by the rate equations. In the system used for this work, the laser is appropriately detuned from the Raman resonance, and the presence of the quadrupole field provides additional Zeeman splitting.

2.3 State Couplings and Rate Calculations

The rate equations include two rates for transitions between any given pair of states: a spontaneous rate γ_{ji}, and a stimulated rate R_{ij}. The spontaneous rate, naturally, depends only on the properties of the atom. The stimulated rate also depends on the optical properties of the incident light, namely intensity, frequency, and polarization.

Both of these rates depend on the degree to which the light field couples the states; this is quantified by a matrix element that is denoted here by μ_{ij}, and whose magnitude squared weights the transition rates. This matrix element is largely determined by angular momentum considerations, and can be derived relatively simply.

2.3.1 Notation

The relationship between the basis characterized by separate angular momenta $\vec{J_1}$ and $\vec{J_2}$, denoted as $|J_1 m_1, J_2 m_2\rangle$, and the basis characterized by the total angular momentum $\vec{J_{12}} = \vec{J_1} + \vec{J_2}$, denoted as $|J_1, J_2; J_{12} m_{12}\rangle$ is usually expressed in terms of the Clebsch-Gordan coefficients $C^{J_{12}m_{12}}_{J_1 m_1, J_2 m_2}$ which are defined as

$$C^{J_{12}m_{12}}_{J_1 m_1, J_2 m_2} = \langle J_1 m_1, J_2 m_2 | J_1, J_2; J_{12} m_{12}\rangle \tag{2.7}$$

A more symmetric way to denote the relationship of these three angular momenta is to use the Wigner $3j$ symbol, defined as[24]

$$C^{J_{12}m_{12}}_{J_1 m_1, J_2 m_2} = (-1)^{-J_1+J_2-m_{12}}\sqrt{2J_{12}+1}\begin{pmatrix} J_1 & J_2 & J_{12} \\ m_1 & m_2 & -m_{12} \end{pmatrix} \tag{2.8}$$

The power of the $3j$ symbol is that the symmetry properties of the Clebsch-Gordan coefficients are represented much more simply. In particular, two columns of the $3j$ symbol can be swapped with the addition of a factor of $(-1)^{J_1+J_2+J_{12}}$. It follows that the value of the $3j$ symbol is invariant under cyclical permutation of its columns.

Now, consider the coupling together of three angular momenta, $\vec{J_1}$, $\vec{J_2}$, and $\vec{J_3}$. One reasonable way to treat this system would be to couple two, say $\vec{J_1}$ and $\vec{J_2}$, into an intermediate angular momentum $\vec{J_{12}}$, using the methods described above, and then couple this intermediate with the third angular momentum $\vec{J_3}$ to get the total angular momentum $\vec{J}$. The result of this process should be independent of the choice of the initial pair, by the associativity of vector addition, so there should be a unitary relationship between the basis $|J_{12}\ J_3;\ J\ m_J\rangle$ and the basis $|J_1\ J_{23};\ J\ m_J\rangle$. This transformation defines the *Wigner 6j* *symbol*:[24]

$$\langle J_1 J_{23}; J m_J | J_{12} J_3; J m_J \rangle = (-1)^{J_1+J_2+J_3+J} \sqrt{(2J_{12}+1)(2J_{23}+1)} \left\{ \begin{array}{ccc} J_1 & J_2 & J_{12} \\ J_3 & J & J_{23} \end{array} \right\} \tag{2.9}$$

The $6j$ symbol also has desirable symmetry properties. Any two columns of the symbol can be swapped without change of value. If two columns of the symbol are inverted, the value also does not change. As with the properties of the $3j$ symbol, these symmetries are very useful in derivations involving angular momenta.

2.3.2 Matrix Element for Fine Structure States

In the $|J m_J\rangle$ basis, the transition matrix element between an excited state j (denoted by primed quantum numbers) and a ground state i (denoted by unprimed quantum numbers) is[25]

$$\mu_{ij} = e \langle n' J' m_J' | \,\hat{\epsilon} \cdot \vec{r}\, | n J m_J \rangle \tag{2.10}$$

where $\hat{\epsilon}$ is the polarization vector of the light.

If we expand Equation 2.10 using Clebsch-Gordan coefficients, we obtain an expression for the matrix element in terms of the more basic S and L angular momentum states. Since the operator $\hat{\epsilon} \cdot \vec{r}$ only couples to the orbital angular momentum L, the spin matrix element $\langle S' m_S' | \,\hat{\epsilon} \cdot \vec{r}\, | S m_S \rangle$ is trivial, and so we get

$$\mu_{ij} = e \sum_{m_L', m_S'} \sum_{m_L, m_S} C^{J' m_J'}_{L' m_L', S' m_S'} C^{J m_J}_{L m_L, S m_S} \langle n' L' m_L' | \,\hat{\epsilon} \cdot \vec{r}\, | n L m_L \rangle \, \delta_{SS'} \delta_{m_S m_S'} \tag{2.11}$$

The dipole transition operator can be rewritten as the product of the radial coordinate operator $|r|$ and a spherical harmonic Y_{1q}, with q being a quantum number denoting the polarization of the light. The radial operator only acts upon the radial wavefunction $|nL\rangle$, and the spherical harmonic only acts on the angular wavefunction $|L m_L\rangle$, so the matrix element decomposes as

$$\langle n' L' m_L' | \,\hat{\epsilon} \cdot \vec{r}\, | n L m_L \rangle = \langle n' L' | \, |r| \, | n L \rangle \langle L' m_L' | \sqrt{\frac{4\pi}{3}} Y_{1q} \, | L m_L \rangle \tag{2.12}$$

The angular part of this matrix element is straightforward to calculate with the properties of spherical harmonics, and can be expressed in terms of the $3j$ symbol as[25]

$$\sqrt{\frac{4\pi}{3}} \langle L' \; m_L' | \, Y_{1q} \, | L \; m_L \rangle = (-1)^{L' - m_L'} \sqrt{2L'+1} \begin{pmatrix} L' & 1 & L \\ m_L' & q & m_L \end{pmatrix} \tag{2.13}$$

assuming that L' is greater than L.

Substituting Equation 2.13 and Equation 2.12 into Equation 2.11, and re-writing all Clebsch-Gordan coefficients and $3j$ symbols as matrix elements gives, with some rearrangement of terms,

$$\mu_{ij} = e \langle n'L' | \, |r| \, |nL\rangle \sum_{m_L, m_S, m'_L} \left(\begin{array}{c} \langle SL; Jm_J | Lm_L, Sm_S \rangle \langle Lm_L, 1q | L1; L'm'_L \rangle \\ \times \langle L'm'_L, Sm_S | L'S; J'm'_J \rangle \end{array} \right) \tag{2.14}$$

The $|L'm'_L\rangle$ states form a complete basis here, and summing over this basis removes it from the expression, leaving the sum

$$\mu_{ij} = e \langle n'L' | \, |r| \, |nL\rangle \sum_{m_L, m_S} \langle SL; Jm_J | Lm_L, Sm_S \rangle \langle Lm_L, Sm_S, 1q | L'S; J'm'_J \rangle \tag{2.15}$$

A similar sum can now be done with the $|Lm_L, Sm_S\rangle$ complete basis, leaving us with a single angular matrix element.

$$\mu_{ij} = e \langle n'L' | \, |r| \, |nL\rangle \langle Jm_J, 1q | L'S; J'm'_J \rangle \tag{2.16}$$

This matrix element cannot be evaluated as written, since the left-hand side is in the $(J, 1)$ intermediate basis, and the right-hand side is in the (L', S) intermediate basis. However, the transformation between these two bases is unitary, as shown in Section 2.3.1, and can be written concisely using a $6j$ symbol. Hence, this matrix element can be written as the product of a $3j$ symbol and a $6j$ symbol.

$$\begin{aligned} \mu_{ij} = {} & e \langle n'L' | \, |r| \, |nL\rangle (-1)^{L+S+J'-J-m'_J} \\ & \times \sqrt{(2J'+1)(2J+1)(2L'+1)} \times \left\{ \begin{array}{ccc} L' & J' & S \\ J & L & 1 \end{array} \right\} \left(\begin{array}{ccc} J & 1 & J' \\ m_J & q & -m'_J \end{array} \right) \end{aligned} \tag{2.17}$$

This equation allows us to calculate the relative transition strengths for the fine structure sublevels of a given line without knowing the radial component of the equation, as the n and L quantum numbers remain the same for all of the fine structure sublevels. The method used in this work is to treat the quantity $e \langle n'L' | \, r \, |nL\rangle$ as the 'total line strength', and divide it out to get the fractional strengths for each transition.

2.3.3 Matrix Element for Hyperfine Structure States

An analogous process can be used to calculate matrix elements for hyperfine structure states. In this case the pertinent matrix element becomes, in the $|Fm_F\rangle$ basis,

$$\mu_{ij} = e\,\langle n'F'm'_F|\,\hat{\epsilon}\cdot\vec{r}\,|nFm_F\rangle \tag{2.18}$$

As with the fine structure matrix element, this matrix element can be expanded, this time in terms of J and I. The I-component of the matrix element has no relation to the orbital angular momentum and is thus trivial, giving

$$\mu_{ij} = e \sum_{m_J,m_I,m'_J} C^{F'm'_F}_{J'm'_J,Im_I} C^{Fm_F}_{Jm_J,Im_I} \langle n'J'm'_J|\,\hat{\epsilon}\cdot\vec{r}\,|nJm_J\rangle \tag{2.19}$$

The third matrix element in Equation 2.19 is the fine structure matrix element defined in Equation 2.10. As such, we can substitute in Equation 2.17, giving (with some rearrangement)

$$\begin{aligned}\mu_{ij} &= e\,\langle n'L'|\,|r|\,|nL\rangle\,(-1)^{1+L+S+J'}\sqrt{(2J+1)(2L'+1)}\begin{Bmatrix} L' & J' & S \\ J & L & 1 \end{Bmatrix} \\ &\times \sum_{m_J,m_I,m'_J} \langle J'I;F'm'_F|Im_I,J'm_J\rangle\,\langle J1;J'm'_J|Jm_J,1q\rangle\,\langle Jm_J,Im_I|J,I;Fm_F\rangle\end{aligned} \tag{2.20}$$

The sums can be evaluated in the same way as in the fine structure case, giving

$$\begin{aligned}\sum_{m_J,m_I,m'_J} \langle J'I;F'm'_F|Im_I,J'm_J\rangle\,\langle J1;J'm'_J|Jm_J,1q\rangle\,\langle Jm_J,Im_I|J,I;Fm_F\rangle \\ = \langle J'I;F'm'_F|1q,Fm_F\rangle\end{aligned} \tag{2.21}$$

The matrix element on the right hand side of Equation 2.21 is of the same form as the angular matrix element in Equation 2.16, and can thus be expanded in the same way in terms of a $3j$ symbol and a $6j$ symbol. Substituting this expansion into Equation 2.20 gives

$$\begin{aligned}\mu_{ij} &= e\,\langle n'L'|\,|r|\,|nL\rangle\,(-1)^{1+L'+S+J+J'+I-F+F'-m'_F} \\ &\times\sqrt{(2J+1)(2J'+1)(2F+1)(2F'+1)(2L'+1)} \\ &\times\begin{Bmatrix} L' & J' & S \\ J & L & 1 \end{Bmatrix}\begin{Bmatrix} J' & F' & I \\ F & J & 1 \end{Bmatrix}\begin{pmatrix} F & 1 & F' \\ m_F & q & -m'_F \end{pmatrix}\end{aligned} \tag{2.22}$$

This has the same form as Equation 4.33 in Metcalf, 1999[25], but has factors of $(-1)^{F'-F}$ and $\sqrt{2L'+1}$ that were neglected there. As with the fine structure matrix element, the radial component of Equation 2.22 can be divided out to find the fractional strength of each possible transition, which will only depend on angular momentum quantum numbers and the polarization of the light.

In the case of spontaneous emission, any polarization of light can be involved. Thus, the three possibilities must be summed over in Equation 2.22. Since the different polarizations are emitted incoherently[2], the matrix elements must also be added incoherently, as

$$|\mu_{ij}|^2 = \sum_q |\mu_{ij}(q)|^2 \tag{2.23}$$

From this, it is straightforward to calculate the spontaneous rate γ_{ij}, given a measurement of the excited state lifetime τ. The total rate of spontaneous emission $\gamma = 1/\tau$ includes all possible ground states a given excited state couples to, so to find the specific rate γ_{ij} the total γ is weighted by the matrix elements $|\mu_{ij}|^2$. Thus, the spontaneous rate is given by

$$\gamma_{ij} = \left(\frac{|\mu_{ij}|^2}{\sum_i |\mu_{ij}|} \right) / \tau \tag{2.24}$$

2.3.4 Calculation of the Stimulated Rate R_{ij}

Unlike the spontaneous rate, which depends only on a single atomic property, the stimulated rate is a function of several input parameters. The incident light intensity naturally affects the stimulated transition rate, as does the energy difference between the light photon energy and the transition resonance energy. In the case of a two-level atom, Allen and Eberly[3] have that the stimulated transition rate R is given by

$$2R = \frac{\mathcal{L}I'}{\tau} = \mathcal{L}I'\gamma \tag{2.25}$$

where $\mathcal{L}$ is a Lorentzian factor related to the light frequency and I' is the ratio of the light intensity relative to the saturation intensity of the atom. We can write down a *saturation parameter* s which is defined as $s = \mathcal{L}I'$.

On resonance, the saturation parameter is given by $s_0 = I' = I/I_0$, where I is the incident intensity and the saturation intensity I_0 is given by[25]

$$I_0 = \frac{\pi hc}{3\lambda^3\tau} \tag{2.26}$$

Away from resonance, this is modified by the Lorentzian resonance parameter $\mathcal{L}$, which for a detuning δ for the stimulated transition rate is given by

$$\mathcal{L} = \frac{1}{1 + 4(2\pi\delta \cdot \tau)^2} \tag{2.27}$$

Combining Equation 2.25 and Equation 2.27, we get

$$R = \left(\frac{I/I_0}{2[1+4(2\pi\delta\cdot\tau)^2]}\right)\gamma \tag{2.28}$$

This equation gives that the transition rate increases without bound as the intensity increases, giving in the limit of infinite power infinite stimulated rates, which distribute the population equally between the states. Equation 2.28 is easily generalized to the case of a multi-level atom by weighting it by the matrix element magnitude squared $|\mu_{ij}|^2$ for each particular pair of states. Since the polarization of the laser light is known and definite, there need not be the same sum over polarizations that is necessary in the case of the spontaneous rate. In the multi-level case the detuning δ also depends on the choice of states, since the states in the ground and excited manifolds are not degenerate.

Chapter 3

Simulation of Optical Pumping Physics

The precise relationship between the excited state population measurement described in Section 1.3 and the nuclear polarization is not directly obvious. A simulation of the optical pumping process can elucidate this relationship, by providing both the variation of the excited state population and the final nuclear polarization for a given set of parameters. These parameters can be used to fit the simulation to the data and thus provide a calculation of the corresponding nuclear polarization.

A simulation based on the rate equations, as defined in Section 2.2.2, is conveniently simple while not approximating away important features of the system. Such a simulation can be made deterministic, which is much more favourable for the use of fitting algorithms than a simulation based on a Monte Carlo method.

3.1 Basic Framework

The rate equations (Equations 2.4 and 2.5) are linear first-order ordinary differential equations, and as such they are fairly straightforward to solve numerically. The simplest way to numerically solve such a system is to use Euler's method[8], defined for a differential equation $y'(x) = f(x, y)$ and initial condition $y(x_0) = y_0$ by the recurrence relation

$$y(x_{n+1}) = y(x_n) + hf(x_n, y(x_n)) \tag{3.1}$$

where h is the increment in x between iterations of the recurrence relation. Equation 3.1 can easily be generalized to a system of equations such as the rate equations, with the replacement of the single dependent variable y with a vector of dependent variables, $\mathbf{y}$. The simplicity of the rate equations ensures that no more complicated numerical method is necessary for an accurate simulation.

The choice of initial conditions for the optical pumping simulation is simplified by the action of the MOT. The randomness of the MOT processes acts to distribute the population evenly through the various hyperfine structure states. There is an interval between the deactivation of the MOT and the activation of the optical pumping that is sufficient for all atoms to decay to the ground state, so the initial excited state population used was zero. Thus, each of the six ground state levels was given an initial population of 1/6.

Since the full circularly-polarized optical pumping process requires two laser beams, as described in Section 2.2.2, the simulation also includes two laser beams, tuned to different frequencies. The stimulated transition rates for these two beams are calculated separately and then added incoherently. The simulation implements a main pumping beam referenced to the $F = 3/2 \rightarrow 3/2$ transition and a repump beam referenced to the $F = 1/2 \rightarrow 3/2$ transition.

Sections 2.3.4 and 2.3.3 describe the calculation of the coefficients in the rate equations for eigenstates of the total angular momentum $\vec{F}$ and its projection m_F. This is the most natural basis in which to consider the problem, but its use is marred by an essential ambiguity: is the quantization axis the direction of the optical pumping light, or is it the direction of the magnetic field? These are not the same; the MOT quadrupole field is kept on during the optical pumping cycle as its switching speed is much slower than that of the optical elements of the experiment. Through most of the trap cloud, the quadrupole field is not aligned with the optical pumping beam and thus provides an off-axis field. The result is both poorer polarization and greater complexity in analysis, but the gains of faster switching speed make this a worthwhile trade-off.

Polarizations in the initial and final states are intended to be referenced to an axis that is well defined with respect to the beta decay experiment. Only the optical pumping axis satisfies this condition, so that axis was selected as the quantization axis. In this case, we must accommodate an off-axis magnetic field, which is a significant effect that acts to spoil a possible perfect polarization. From a semiclassical perspective, the magnetic moment and thus the spin of the atom will precess around the magnetic field axis. Since this direction is not the same as the quantization direction, the projection of the angular momentum will change over time as the spin precesses.[23] A simple semiclassical model of Larmor precession was found to have inadequate theoretical backing, so a full quantum mechanical treatment was developed instead. This more accurate model requires abandoning the simple $|F, m_F\rangle$ basis for a new basis that depends on the off-axis magnetic field.

3.2 A New Basis for Optical Pumping

The Hamiltonian for an angular momentum $\vec{S}$ in a general magnetic field is given by

$$H = -\vec{\mu} \cdot \vec{B} = -g\mu_B \vec{S} \cdot \vec{B} \qquad (3.2)$$

We can without loss of generality define the direction of the optical pumping light as the z-axis, and the plane shared by the optical pumping light and the magnetic field vector as the x-z plane, so that the magnetic field can be written as

$$\vec{B} = B_0\hat{z} + B'\hat{x} \tag{3.3}$$

and thus the Hamiltonian can be written in terms of spin matrices as

$$H = -g\mu_B(B_0 S_z + B' S_x) \tag{3.4}$$

For a given spin, this is a relatively simple matrix with diagonal terms proportional to B_0 and off-diagonal terms proportional to B'. The two cases that are relevant for the ^{80}Rb $5S_{1/2}$ and $5P_{1/2}$ states used in the optical pumping process are spin 1/2 and spin 3/2. For spin 1/2, the Hamiltonian matrix is then, from the usual Pauli matrices,

$$H = -\frac{1}{2}g\mu_B\left(B_0\begin{bmatrix} 1 & 0 \\ 0 & -1 \end{bmatrix} + B'\begin{bmatrix} 0 & 1 \\ 1 & 0 \end{bmatrix}\right) = -\frac{1}{2}g\mu_B\begin{bmatrix} B_0 & B' \\ B' & -B_0 \end{bmatrix} \tag{3.5}$$

For spin 3/2, the Hamiltonian is more difficult to write down due to the larger matrices involved. The spin matrix S_z is a straightforward diagonal matrix as the initial basis consists of its eigenstates; we have

$$S_z = \frac{1}{2}\begin{bmatrix} 3 & 0 & 0 & 0 \\ 0 & 1 & 0 & 0 \\ 0 & 0 & -1 & 0 \\ 0 & 0 & 0 & 3 \end{bmatrix} \tag{3.6}$$

To find S_x, we use the relation $S_x = 1/2(S_+ + S_-)$, since we know the form of S_+ and its Hermitean conjugate S_- from the equation $S_+\left|J,m\right\rangle = \sqrt{J(J+1) - m(m+1)}\left|J,m+1\right\rangle$[21]. Thus we have

$$S_+ = \begin{bmatrix} 0 & \sqrt{3} & 0 & 0 \\ 0 & 0 & \sqrt{4} & 0 \\ 0 & 0 & 0 & \sqrt{3} \\ 0 & 0 & 0 & 0 \end{bmatrix}, S_x = \begin{bmatrix} 0 & \sqrt{3/4} & 0 & 0 \\ \sqrt{3/4} & 0 & 1 & 0 \\ 0 & 1 & 0 & \sqrt{3/4} \\ 0 & 0 & \sqrt{3/4} & 0 \end{bmatrix} \tag{3.7}$$

Therefore, we can write the Hamiltonian for spin 3/2 as

$$H = -g\mu_b \begin{bmatrix} \frac{3}{2}B_0 & \sqrt{\frac{3}{4}}B' & 0 & 0 \\ \sqrt{\frac{3}{4}}B' & \frac{1}{2}B_0 & B' & 0 \\ 0 & B' & -\frac{1}{2}B_0 & \sqrt{\frac{3}{4}}B' \\ 0 & 0 & \sqrt{\frac{3}{4}}B' & -\frac{3}{2}B_0 \end{bmatrix} \tag{3.8}$$

The Hamiltonians described in Equations 3.5 and 3.8 can, for a given choice of B_0 and B', be numerically diagonalized to find a new basis in which to simulate the optical pumping process. The basis described by the normalized eigenvectors naturally accounts for the off-axis magnetic field and its polarization-spoiling effects.

This process makes a significant approximation, namely that the $F = 1/2$ and $F = 3/2$ hyperfine sublevels do not mix. The hyperfine splittings of the two states, as shown in Table 3.2, are relatively large, especially in the ground state. The magnetic fields in this system are on the order of 1 G, which results in a Zeeman splitting on the order of 1 MHz. This is much less than the ground state hyperfine splitting of approximately 230 MHz or even the excited state hyperfine splitting of about 30 MHz. In systems with smaller hyperfine splittings, this approximation would be invalid and a combined, block diagonal Hamiltonian would have to be used instead. The same eigenvectors are used for both the ground and excited states, as the only difference in the Zeeman Hamiltonian is the g-factor, which as a multiplicative constant only affects the eigenvalues.

3.3 Translation into the New Basis

The use of this new basis requires that the physical quantities calculated in Chapter 2 be transformed from functions of F and m_F to values corresponding to the new states. As the relation between the two bases is unitary, this is a relatively straightforward process.

3.3.1 Energies in the New Basis

The Hamiltonians in Equations 3.5 and 3.8 break the degeneracy of the m_F states at the same time as they mix them. This is the familiar Zeeman effect, given by the eigenvalues of the magnetic Hamiltonian corresponding to the eigenvectors that describe the new states.

To calculate the eigenvalues, we must know the g-factor that multiplies the Hamiltonian matrix. The g-factor is a function of the angular momenta and thus is different for the four hyperfine levels in the system. Foot, 2005[13] relates the g-factor for a hyperfine structure state, g_F, to the g-factor for the corresponding fine structure state, g_J, by

$$g_F = g_J \frac{\langle \mathbf{J} \cdot \mathbf{F} \rangle}{F(F+1)} = g_J \frac{F(F+1) + J(J+1) - I(I+1)}{2F(F+1)} \tag{3.9}$$

This equation assumes that the contribution from the nuclear magnetic moment is negligible, and thus the nuclear angular momentum I only enters in the transformation from g_F to g_J and does not contribute to the g-factor on its own. It is also straightforward to calculate the fine structure g-factor g_J from its constituent angular momenta. Both the spin and orbital angular momenta have known g-factors, which are related to the combined g-factor as[25]

$$g_J = \frac{\langle \mathbf{L} \cdot \mathbf{J} \rangle + g_S \langle \mathbf{S} \cdot \mathbf{J} \rangle}{J(J+1)} \approx 1 + \frac{J(J+1) + S(S+1) - L(L+1)}{2J(J+1)} \tag{3.10}$$

The right hand side of Equation 3.10 approximates the electron g-factor g_S to be exactly 2, an approximation correct to one part per thousand.

3.3.2 Rates in the New Basis

The rates of transition between the states, as calculated in Section 2.3, are dependent on the transition matrix element $|\langle n'F'm_F'|\,\hat{\epsilon}\cdot\vec{r}\,|nFm_F\rangle|^2$, for a ground state $|nFm_F\rangle$ and an excited state $|n'F'm_F'\rangle$. Those matrix elements were calculated in the original basis and in that basis the calculation was relatively straightforward. Since the new states are related to the old states by a unitary transformation, the conversion into the new basis is also straightforward.

We can write the states in the new basis as

$$|nFq\rangle = \sum_{m_F} K_{F,m_F,q}\, |nFm_F\rangle \tag{3.11}$$

where $K_{F,m_F,q}$ are real constants corresponding to the values in the normalized eigenvector, and q is an arbitrary label for the states in the new basis. Thus, the matrix element between the ground state $|nFq\rangle$ and the excited state $|n'F'q'\rangle$ is given by

$$\mu_{ij} \equiv e \langle n'F'q'|\,\hat{\epsilon}\cdot\vec{r}\,|nFq\rangle = e \sum_{m_F, m_F'} K_{F',m_F',q'} K_{F,m_F,q} \langle n'F'm_F'|\,\hat{\epsilon}\cdot\vec{r}\,|nFm_F\rangle \tag{3.12}$$

This matrix element's magnitude squared can be used with Equations 2.24 and 2.28 to weight the stimulated and spontaneous rates in the same way as the matrix elements in the original basis.

Since the states in the new basis have mixed angular momentum, two of those states can be coupled by more than one polarization of light. Generally, this only affects spontaneous emission, as for excitation and stimulated emission the light polarization is specified. For spontaneous emission, the rates add incoherently as the different polarizations do not interfere with each other.

3.3.3 Power Shaping

Ideally, the optical pumping cycle should begin with the laser already at its full power. In practice, though, it takes a finite amount of time for the laser to 'switch on', and in this time it will have decreased power. In the system used in the experiment, the optical pumping laser is switched on and off using an acousto-optic modulator (AOM), which has a switching time on the order of 100 ns.

Thus, for the first 200–300 ns of the simulation, the power must be modulated to accurately match the data. Measurements made of the laser power as a function of time as the AOM switches on[6] suggest that the modulation should be of the form

$$P(t) = P_0 \frac{1}{1 + A \exp[-t/\tau]} \tag{3.13}$$

The best fits to those measurements give that $A = 9.025$ and $\tau = 38.5$ns.

3.4 Polarization of System

The polarization that is of interest in this case is not the total atomic polarization $\langle m_F \rangle / F$, but the nuclear polarization $\langle m_I \rangle / I$. The former is trivial to calculate in the initial basis as the states are eigenstates of m_F, but the calculation of the nuclear polarization is more complicated as m_I is not a good quantum number. Nevertheless, the orthogonality of the $|J, m_J\rangle$ states allows the calculation of the nuclear polarization to remain straightforward in practice.

For a given m_F eigenstate, the expectation value $\langle m_I \rangle$ can be written as

$$\langle F m_F | \, m_I \, | F m_F \rangle = \sum_{m_J, m'_J, m_I, m'_I} \left[\begin{array}{l} C^{F m_F}_{J m_J, I m_I} C^{F m_F}_{J m'_J, I m'_I} \langle J m_J, I m_I | \, m_I \, | J m'_J, I m'_I \rangle \\ \times \, \delta_{m_F, m_I + m_J} \delta_{m_F, m'_I + m'_J} \end{array} \right] \tag{3.14}$$

Since the m_I operator does not act upon the $|J, m_J\rangle$ components of the two states, the orthonormality of those states requires that $m_J = m'_J$. Similarly, the m_I operator is clearly diagonal in the space described by the $|I, m_I\rangle$ components and so the polarization is given by

$$\langle F m_F | \, m_I \, | F m_F \rangle = \sum_{m_I, m_J} m_I \left(C^{F m_F}_{J m_J, I m_I} \right)^2 \delta_{m_J, m_F - m_I} \tag{3.15}$$

We can then translate this into the $|Fq\rangle$ basis in the same manner, with the unitary transformation coefficients $K_{F,m_F,q}$ appearing in the same manner as the Clebsch-Gordan coefficients above:

$$\langle m_I \rangle \equiv \langle Fq|\, m_I \,|Fq\rangle = \sum_{m_F,m_I,m_J} m_I \left(K_{F,m_F,q}\right)^2 \left(C^{Fm_F}_{Jm_J,Im_I}\right)^2 \delta_{m_J,m_F-m_I} \tag{3.16}$$

Once this expectation value is calculated, the total polarization can be calculated by normalizing to the total I.

The calculation of the tensor alignment is analogous to that of the vector polarization, with m_I replaced by ${m_I}^2$. Unlike the vector polarization, though, the tensor alignment is not simply $\langle {m_I}^2 \rangle$ scaled by the total angular momentum, but comes in with a form that is useful for Cartesian tensors,

$$T = \frac{I(I+1) - 3\langle {m_I}^2 \rangle}{I(2I-1)} \tag{3.17}$$

3.5 Known ^{80}Rb Atomic Structure

To accurately simulate the optical pumping process, several of the atomic properties of ^{80}Rb must be known. The wavelength of the optical pumping light is needed to calculate the saturation intensity (Equation 2.26). The excited state lifetime determines the width of the Lorentzian profile for calculating stimulated rates, and also the scale of all of the transition rates. Finally, the hyperfine splittings must be known to calculate the detunings of the two pumping beams from the various resonances and thus determine where in the line profile the light sits. These values are summarized in Table 3.2 below.

We define the *hyperfine constant* as the constant of proportionality in the hyperfine Hamiltonian, which arises from the interaction of the nuclear magnetic moment, proportional to the nuclear angular momentum $\vec{I}$, with the effective magnetic moment of the electron, proportional to its total angular momentum $\vec{J}$. For the $J = 1/2$ case considered here, this is a pure dipole-dipole interaction with no contribution from higher moments of the nucleus, and we get a Hamiltonian of the form

$$H = A(\vec{I} \cdot \vec{J}) \tag{3.18}$$

This is a simpler and more general way to express hyperfine structure than in terms of the explicit hyperfine splittings. The hyperfine splitting for a pair of states is related to the difference between the value of $\vec{I} \cdot \vec{J}$ for those states by the hyperfine constant. From the

Isotope and State	Hyperfine Constant (MHz)
^{85}Rb $5S_{1/2}$	$1011.910813 \pm 3 \times 10^{-6}$[34]
^{85}Rb $5P_{1/2}$	120.645 ± 0.005[11]
^{87}Rb $5S_{1/2}$	3417.3413[4]
^{87}Rb $5P_{1/2}$	406.119 ± 0.007[11]

Table 3.1: Hyperfine Constants of ^{85}Rb and ^{87}Rb

equation $\vec{F} = \vec{I} + \vec{J}$, we have that

$$\vec{I} \cdot \vec{J} = \frac{1}{2}(F(F+1) - I(I+1) - J(J+1)) \tag{3.19}$$

and so the energy difference between two states of different F and equal I and J is given by

$$\Delta E = \frac{1}{2}A(F_1(F_1+1) - F_2(F_2+1)) \tag{3.20}$$

where $F_1 > F_2$. Thus, for the $5S_{1/2}$ and $5P_{1/2}$ states of ^{80}Rb which have sublevels with $F = 3/2$ and $F = 1/2$, the hyperfine splitting is 3/2 of the hyperfine constant, i.e. $\Delta E = (3/2)A$.

Thibault et al.[32], give the value of the hyperfine constant for the ^{80}Rb ground state as (-155.957 ± 0.002) MHz, which gives a splitting of (-233.936 ± 0.003) MHz between the two ground state hyperfine levels. In the case of the excited state, though, there is no analogous measurement of the hyperfine constant. Thus, we must estimate it using other available data.

Ignoring the hyperfine anomaly, the ratio of ground and excited hyperfine constants should be the same for all isotopes of the same element, i.e.

$$\frac{A_{5P_{1/2}}(80)}{A_{5S_{1/2}}(80)} \approx \frac{A_{5P_{1/2}}(85)}{A_{5S_{1/2}}(85)} \approx \frac{A_{5P_{1/2}}(87)}{A_{5S_{1/2}}(87)} \tag{3.21}$$

Thus, the excited state hyperfine constant can be estimated from the ground and excited state hyperfine constants of stable ^{85}Rb and/or ^{87}Rb, along with the ground state hyperfine constant of ^{80}Rb. The hyperfine constants for ^{85}Rb and ^{87}Rb are very well measured; these measurements are summarized in Table 3.1.

Using the data from ^{85}Rb, this gives the hyperfine constant for the $5P_{1/2}$ excited state of ^{80}Rb as (-18.5940 ± 0.0008) MHz. For the data from ^{87}Rb, the ^{80}Rb hyperfine constant is calculated as (-18.5340 ± 0.0003) MHz. These are not consistent with each other, but since the process for calculating these is approximate, this is not disastrous. The discrepancy is less than one part per thousand, which is small enough not to cause problems. The average of these two values, (-18.5640 ± 0.0009) MHz was used for this work. From this,

Wavelength of D1 transition (vac.)	795.0 nm [1]
Lifetime of $5P_{1/2}$ state	27.64 ns [29]
Ground state ($5S_{1/2}$) hyperfine splitting	(-233.936 ± 0.003) MHz
Excited state ($5P_{1/2}$) hyperfine splitting	(-27.846 ± 0.001) MHz

Table 3.2: Atomic Properties of ^{80}Rb

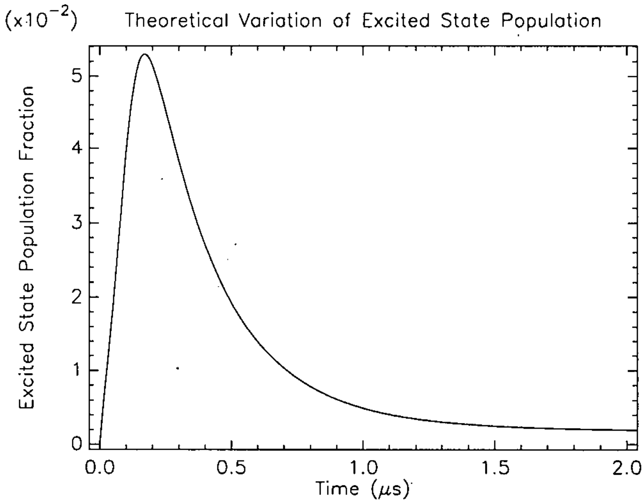

Figure 3.1: Typical simulation result

the hyperfine splitting of the excited state was calculated to be (-27.846 ± 0.001) MHz.

3.6 Fitting Simulation to Data

The most important output of the optical pumping simulation is the total excited state population as a function of time. As described in Section 1.3, the shape of this function is highly dependent on the degree of polarization achieved over the course of the process. Figure 3.1 shows the excited state population for a typical simulated optical pumping run.

At the same time as the simulation produces the excited state population, it also determines the polarization of the simulated atoms at that given time. As this output polarization depends on time, it is important to choose the correct time to read off the final polarization value. Figure 3.2 shows the variation of both positive and negative polarization with time. As can be seen there, the polarization reaches a stable value fairly early on, and continues in a steady state for the rest of the simulated time interval. As such, the simulation reports the polarization value as the value at the final timestep.

Importantly, the simulation can also be run so that it simulates hyperfine pumping rather than full optical pumping. This is accomplished in the simulation, as in the laboratory, by

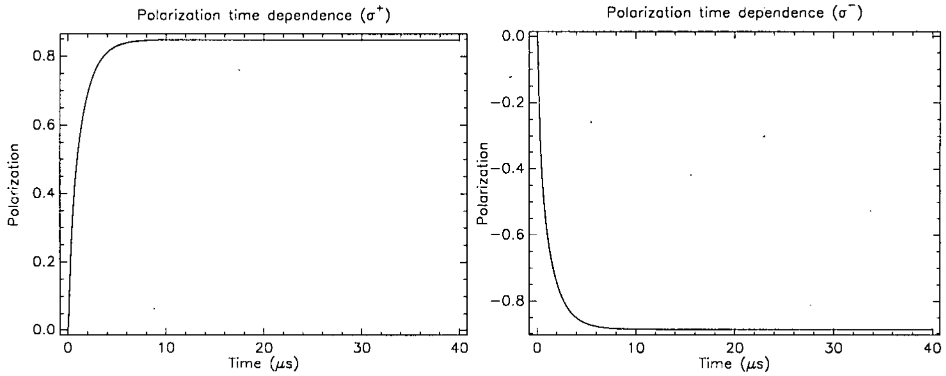

Figure 3.2: Positive and negative polarization time dependence

setting the power of the repump beam to zero. The resulting population curve is mainly a function of the power of the remaining beam.

For the purposes of fitting the simulation output to the data, a fitting routine based on the Marquart algorithm as described in the book Numerical Recipes in Fortran[27] was used. A custom fit routine was necessary to interface properly with the optical pumping simulation and its nonlinear relationship with its parameters.

The Marquart algorithm, like any other fitting algorithm, works by numerically minimizing the goodness-of-fit function, χ^2. The location in the parameter space can be written as a parameter vector $\mathbf{a}$; the fit algorithm determines a series of increments $\delta\mathbf{a}$ so as to converge on that minimum. The data is denoted here as a series of points (x_i, y_i), and the fit function as $y(\mathbf{a}, x_i)$.

The formalism of the fit algorithm is centred on the curvature matrix α_{kl}, defined as

$$\alpha_{kl} = \frac{1}{2}\frac{\partial^2\chi^2}{\partial a_k \partial a_l} = \sum_i \frac{1}{\sigma_i{}^2}\left[\frac{\partial y(\mathbf{a}, x_i)}{\partial a_k}\frac{\partial y(\mathbf{a}, x_i)}{\partial a_l} - (y_i - y(\mathbf{a}, x_i))\frac{\partial^2 y(\mathbf{a}, x_i)}{\partial a_k \partial a_l}\right] \tag{3.22}$$

where σ_i is the error on y_i, which for the y_i used in this thesis is a Poisson error. The curvature matrix appears in the Taylor series of χ^2 as $\alpha_{kl}a_k a_l$. Approximating χ^2 by the terms up to and including this quadratic term, we find the other quantity used in determining the parameter increments to be the gradient of the χ^2, β_k, defined as

$$\beta_k = -\frac{1}{2}\frac{\partial\chi^2}{\partial a_k} = \sum_i \frac{(y_i - y(\mathbf{a}, x_i))}{\sigma_i{}^2}\frac{\partial y(\mathbf{a}, x_i)}{\partial a_k} \tag{3.23}$$

Using the quadratic form approximation of χ^2, the ideal parameter step $\delta\mathbf{a}$ can be calculated as

$$\alpha_{kl}\delta a_l = \beta_k \tag{3.24}$$

Thus, the most basic framework for a fitting algorithm based on this formalism is to calculate α_{kl} and β_k with numerical derivatives, and then invert the matrix to solve Equation 3.24.

Since α_{kl} only affects the steps taken and not the final result, it can be used in whatever form is convenient for efficient convergence. The second derivative term contributes significantly less to the value of the curvature matrix than the cross term, since it is multiplied by the residual $(y_i - y(\mathbf{a}, x_i))$, which tends to zero for a successful fit function. It is also more difficult to calculate than the first derivative terms and has been found to cause instability due to its greater sensitivity to statistical fluctuations in the data. Thus, it is in practice omitted and the curvature matrix has the simpler form

$$\alpha_{kl} = \sum_i \frac{1}{{\sigma_i}^2} \left[\frac{\partial y(\mathbf{a}, x_i)}{\partial a_k} \frac{\partial y(\mathbf{a}, x_i)}{\partial a_l} \right] \tag{3.25}$$

Two more modifications to α_{kl} are made for greater stability. The different orders of magnitude of the parameters are normalized away by dividing each α_{kl} by the diagonal elements $\sqrt{\alpha_{kk}\alpha_{ll}}$ for the inversion of the matrix, with an analogous transformation restoring the proper magnitude for use in Equation 3.24. Also, the choice of σ_i used was not the simple $\sqrt{y(\mathbf{a}, x_i)}$, but rather $y(\mathbf{a}, x_i)/\sqrt{y_i}$, which is almost identical to the standard Poisson choice near to equilibrium but which deals better with data points that are zero.

Marquart's addition to this method aims to curtail divergences when far from the equilibrium by adding a floating scale factor to the matrix α_{kl}. This factor, usually denoted as λ, is added to the matrix by multiplying the diagonal terms by $(1 + \lambda)$. Far from convergence, a large value of λ will force α_{kl} to be diagonally dominant, thus allowing for the simpler behaviour of just following the gradient until a decrease in the χ^2 is found. The result is that the algorithm becomes markedly less sensitive to the initial guess. The procedure for adjusting λ is simple: increase it by a factor of ten if the calculated step increases the χ^2, and decrease it by a factor of ten if the χ^2 decreases.

Once the value of χ^2 reaches a suitable convergence point, the uncertainties in the fit parameters can be found from the covariance matrix $C_{kl} = {\alpha_{kl}}^{-1}$. The uncertainty in each parameter a_k is then $\sqrt{C_{kk}}$.

Chapter 4

Results

In December 2005, the TRINAT group was allocated two weeks of ^{80}Rb beam from ISAC. During this time, the data for the final asymmetry measurement was taken. This chapter will describe the application of the methods described in the previous chapter to this data, and the results thus obtained. A rough method of estimating the polarization will be developed to help verify these results, and the various sources of error will be examined.

4.1 Choice of Data

All of the analysis was performed using only data from the second week of the run. From a statistical perspective this is disadvantageous as compared to using the full data set, but differences in setup between the two weeks favour the data from the second week for systematic error analysis.

During the first week, the same optical pumping frequency was used with both polarizations, which due to differences in the atomic response caused the trap to move differently during the optical pumping process. As a result, the trap was in a different final position for positive polarization than it was for negative polarization. During the second week, the frequencies were tuned separately such that the trap position was as consistent as possible between the two polarizations. This change greatly improves the accuracy of the recoil asymmetry measurement, as a difference in trap position between the two polarization states will produce a false asymmetry, masking possible effects from tensor interactions. The 1 mm shift observed in the first week produces a false asymmetry of about 0.04, which is a very large correction.

The second week data was taken with a lower count rate. This greatly improved the performance of the germanium gamma-ray detector which had severe pile-up problems at the higher count rate. The lower population in the neutralization and collection chamber also decreased the gamma-ray background, and lead shielding was placed around the germanium detector to further reduce background. The trap, holding fewer atoms, was more compact, which provides an additional advantage. The net result is a data set that, while smaller, is significantly cleaner.

It is also the case that the timing electronics for the germanium detector were only refined to a useful level during the second week; this is not important for this work, but is important for some of the other data analysis for the experiment.

4.2 Power Measurements with Hyperfine Pumping

During the run of the experiment, several hours of data were taken with the laser sideband switched off, observing the process of hyperfine pumping rather than that of optical pumping. The intent was to directly measure the incident laser power at the trap, as the time dependence of the hyperfine pumping process is largely independent of other physical parameters such as magnetic field and light polarization. As the hyperfine pumping process is fast, the excited state population stays small and the count rate of photoions during the pumping process is correspondingly low. Fitting to these peaks given the statistical fluctuations is difficult, but fortunately the power need not be measured to high accuracy for a sufficiently accurate polarization measurement.

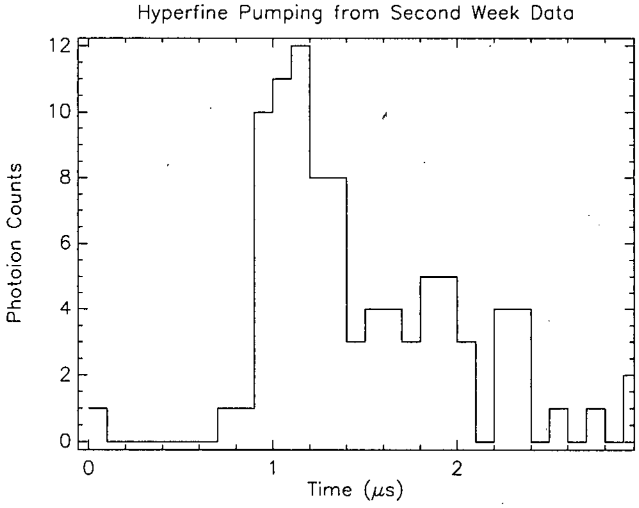

Figure 4.1: Example measurement of hyperfine pumping population curve

A typical dataset is shown in Figure 4.1. This graph represents about four hours of data and contains about 90 counts, including background. The low-statistics nature of this spectrum causes the normal fit algorithm described in Section 3.6 to fail, overwhelmed by statistical fluctuations. To improve the statistics of this measurement, the data for the two circular polarizations was added together. Since the amount of data is approximately the same for both polarizations, the simulation result for the two polarizations was also added together directly. As the polarization measurement is relatively insensitive to the input power, a simple analytic method was used to estimate the power and its uncertainty.

Theoretical population curves were calculated at 1 mW/cm^2 intervals from 1 mW/cm^2

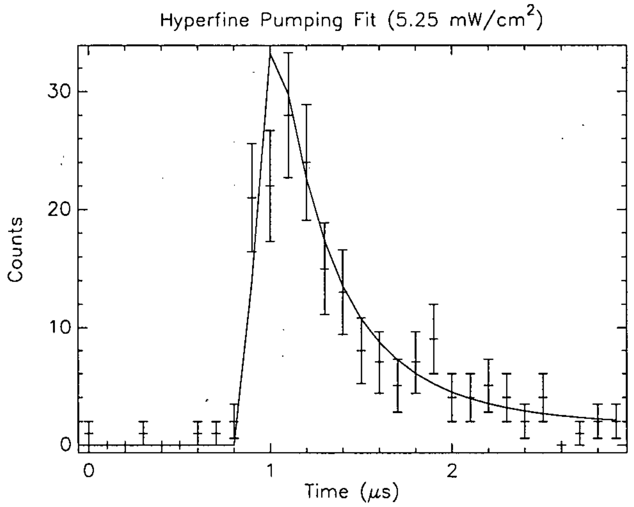

Figure 4.2: Fit to hyperfine pumping data ($\chi^2/n = 0.97$)

to 10 mW/cm^2. Each of these curves was fit to the data using a floating normalization factor and the χ^2 of each fit was evaluated. Since the value of the normalization factor does not affect the power measurement, the use of a χ^2 fit does not bias the result. Further power values were examined around the apparent centroid, and the eventual best fit was for 5.25 mW/cm^2, shown in Figure 4.2. A graph of χ^2 versus power was produced to determine the error on this measurement. These values of χ^2 are shown in Figure 4.3, with the dotted line marking $\chi^2 = {\chi^2}_{min} + 1$. From this plot, an error of ±1.3 mW/cm^2 was determined, giving a measurement of the total incident power of (5.3 ± 1.3) mW/cm^2. The asymmetry of the χ^2 plot is reasonable, as the pumping rate becomes increasingly insensitive to the incident power above the saturation intensity of 1.8 mW/cm^2.

In the full optical pumping case, this power is divided between the two laser frequencies used for pumping and repumping. In this case, the ratio of the two powers was measured using a scanning Fabry-Perot interferometer. This instrument was used to produce a real-time plot of intensity as a function of frequency. An example plot is shown in Figure 4.4. The ratio of the powers in the two frequency bands is then just the ratio in the heights of the resultant peaks.

During the period when the data used for polarization measurements was taken, four measurements of this ratio were made. These measurements can be found in Table 4.1. The mean value of the ratio found from this data is 0.28, with standard deviation 0.01. This value was used in the optical pumping fits described below.

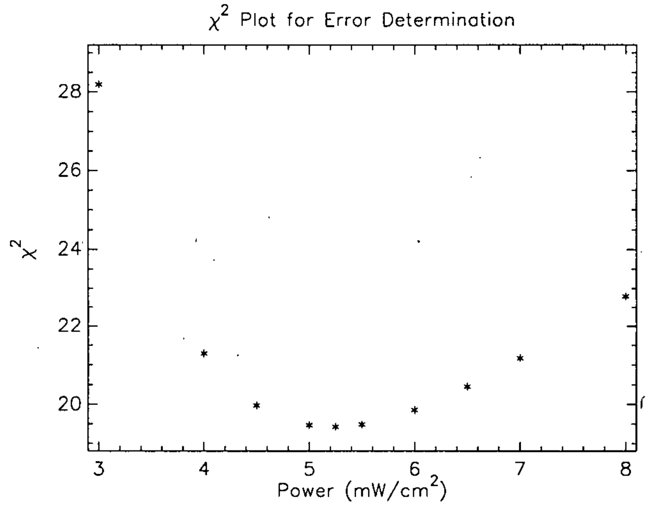

Figure 4.3: χ^2 plot for hyperfine pumping fit

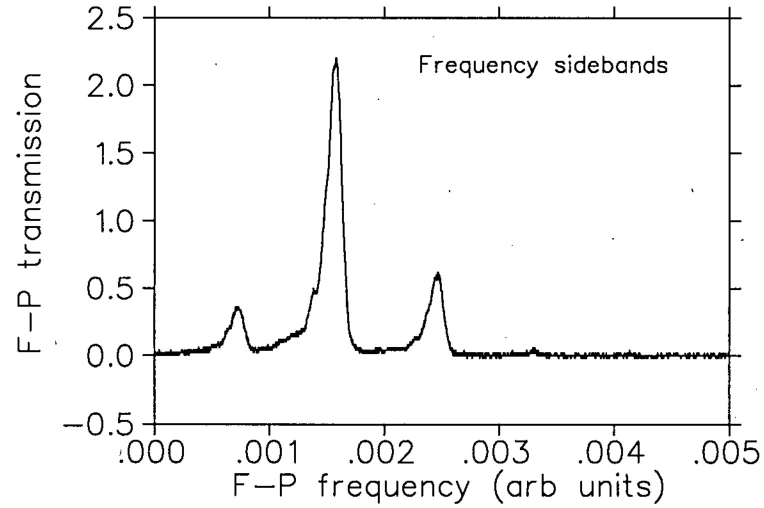

Figure 4.4: Example of Fabry-Perot power spectrum

Run #	Ratio
1136	0.275
1149	0.280
1168	0.296
1183	0.274

Table 4.1: Measurements of relative sideband intensity

4.3 Rough Polarization Estimates

The polarization can be estimated from the peak-to-tail ratio of the population curve, to verify the correctness of the more precise measurement using the optical pumping model. This cross-check depends on none of the assumptions used by the model, and as such is an independent measure of the content of the data.

We can consider the excited state population we measure to be proportional to the ground state population outside the fully-stretched $m_F = \pm 3/2$ state. Initially, this fraction will be 5/6, as the operation of the MOT distributes the population evenly between the six $|F, m_F\rangle$ states. Thus, we can write the final population fraction outside the fully-stretched state, x, as

$$x = \frac{5}{6} r \tag{4.1}$$

where r is the ratio of the final excited state population to the peak excited state population as measured from the population curve.

At this point, several simplifying assumptions must be made. We assume that the final ground state population is only distributed through the half of the manifold with the 'correct' angular momentum sign: the $m_F = 3/2$ state and the two $m_F = 1/2$ states for σ^+ light, for example. The nuclear polarizations of the $F = 3/2$ and $F = 1/2$ states with $m_F = 1/2$ are different, the $F = 3/2$ state having polarization 1/3 and the $F = 1/2$ state having polarization 2/3; this necessitates some estimation of the ratio in population between these states.

In the steady state found in the tail of the population curve, we would expect the population in those states to be in proportion to the strengths of the two transitions from the $m_F = 3/2$ excited state. The transition has twice the strength to the $F = 1/2$ ground state as to the $F = 3/2$ ground state, so the population of the $F = 1/2$ ground state should be twice that of the $F = 3/2$ ground state. Thus the polarization contribution from the fraction of the population in these states, x, is $(2/3 * 2/3 + 1/3 * 1/3)x$ or $5/9x$. The population $(1 - x)$ that is in the fully-stretched state is fully polarized, and so the approximate polarization is given by

$$P \approx (1 - x) + 5/9x = 1 - 4/9x = 1 - 20/27r \tag{4.2}$$

Applying this formula to the experimental data, we find that optical pumping with σ^+ light gives a polarization of approximately 0.86, while σ^- light gives the polarization as approximately 0.89. As we will see below, these values are in remarkably good agreement with those found using the more detailed simulation.

4.4 Frequency Measurements

The frequency of the optical pumping laser is set to a known value by locking it to the $F = 3 \longrightarrow 3$ transition of ^{85}Rb, using saturation spectroscopy[31]. This reference is offset from the actual laser frequency by an acousto-optic modulator (AOM) tuned to shift the frequency from the ^{85}Rb transition to those of ^{80}Rb. As this is a double-pass AOM, the frequency change to the light is twice the AOM driving frequency. An additional AOM is placed between the laser and the vacuum chamber, which is switched on and off to chop the laser on and off.

The switching AOM is held constant at a frequency of 131 MHz. This frequency cancels in the detuning calculation as it is the same for both the resonance and detuned settings of the double-pass AOM. The ^{80}Rb $F = 3/2 \longrightarrow 3/2$ resonance was found by sweeping this AOM over the line profile, observing the final position of the trap and thus the net optical force, and then fitting a Lorentzian to the data points; the AOM frequency of the resonance was found to be $\nu_{3/2 \rightarrow 3/2} = (396.1 \pm 0.4)$ MHz[6]. This result is approximately 10 MHz larger than a previous measurement of the isotope shift found in the literature[32].

As a large optical force on the atoms during the optical pumping cycle causes them to move away from the detection region after pumping, the optical pumping beam is detuned from the resonance. This detuning was adjusted separately for the two circular polarizations to match up the post-pumping position of the atom cloud. The AOM driving frequency that implements this was found to be stable to within 0.3 MHz over the length of the run. The σ^+ light was run with an AOM frequency of $\nu_{AOM} = 398.5$ MHz and the σ^- light was run with an AOM frequency of $\nu_{AOM} = 395.4$ MHz.

Sidebands were produced in the laser's output by injecting an RF signal into the laser diode. The sidebands are produced at integer multiples of the RF frequency away from the central carrier frequency. This sideband is used as a repump beam as described in section 2.2.2. The splitting frequency of $\delta\nu_{light} = -232.1$ MHz was stable to within 0.1 MHz, and is different than the state splitting of $\delta\nu_{atom} = -233.9$ MHz to avoid the coherent effects described in Section 2.2.3.

Thus, we can write the detunings δ_1 and δ_2 from the $F = 3/2 \longrightarrow 1/2$ and the $F = 3/2 \longrightarrow 3/2$ transitions, respectively, as

$$\begin{aligned} \delta_1 &= 2(\nu_{AOM} - \nu_{3/2 \rightarrow 3/2}) + (\delta\nu_{atom} - \delta\nu_{light}) \qquad (4.3) \\ \delta_2 &= 2(\nu_{AOM} - \nu_{3/2 \rightarrow 3/2}) \qquad (4.4) \end{aligned}$$

4.5 Polarization Measurements

Given the above measurements of power and frequency, the polarization can now be measured from the excited state population curve. As shown above, the total power was measured to be (7 ± 3) mW/cm^2, and the ratio of power in the two beams is (0.28 ± 0.01), and the detunings can be calculated using Equations 4.3 and 4.4. The only parameter that remains to be determined is the value of the on-axis magnetic field.

The on-axis magnetic field was produced mainly by a set of trim coils, which are independent of the MOT quadrupole field. These trim coils are used to position the trap while also providing a magnetic field reference for the optical-pumping. If the MOT laser beams were balanced, this field would be zero as the MOT forms at the magnetic field zero. These beams were deliberately attenuated so as to displace the atoms from the centre of the chamber, and the current in the trim coils was adjusted so as to to push the atoms back. These coils were powered with 6.0 A of current during the run, which is larger than the current used when the calibration measurement of was made. The resulting magnetic field was estimated to be 2.4 G by simple linear extrapolation of the calibration.

The error on the magnetic field is determined mainly by the finite size of the trap. While the simulation treats the trap as pointlike with a constant magnetic field throughout, the actual trap has a full width at half maximum of approximately 2 mm. The magnetic field gradient in the vicinity of the trap is about 5 G/cm, so the inherent uncertainty in the magnetic field associated with the finite trap size is ±0.5 G.

The direction of the magnetic field was also measured using a simple device, consisting of a bar magnet mounted to swivel freely in three dimensions. By measuring the field at various locations around the vacuum chamber, the direction of the magnetic field along the optical pumping axis was found to be parallel to the optical pumping beam.

The fit routine uses the off-axis magnetic field as its polarization-spoiling fit parameter, leading to a two-parameter fit including B_x and a multiplicative normalization. The fit generates statistical errors for both of these parameters through the method described in Section 3.6. The error on the polarization-spoiling parameter B_x is translated into an error in the polarization through further runs of the simulation at $(B_x \pm \delta B_x)$. The polarization values so obtained are taken as the upper and lower statistical limits on the polarization.

4.6 Systematic Error Analysis

Uncertainties in the input parameters contribute alongside the statistics of the fit to the uncertainty of the final polarization measurement. While uncertainties in the atomic properties (Section 3.5) are very small (less than a part per thousand), and will not be propagated,

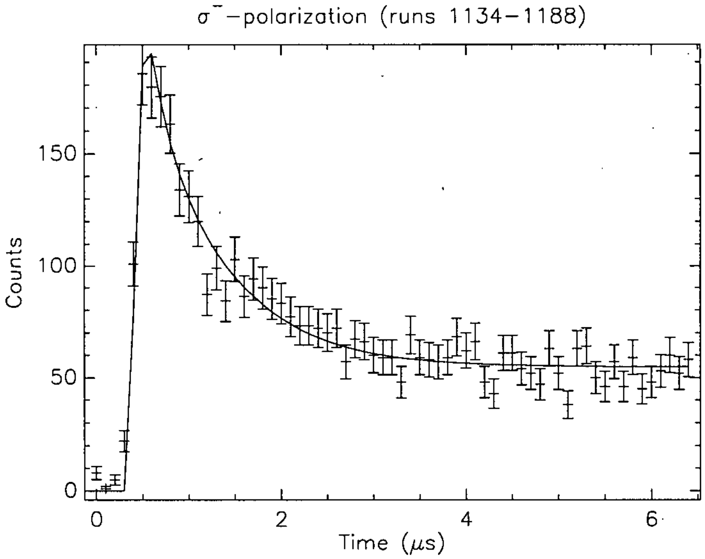

Figure 4.5: Fit to second-week data (σ^- polarization) ($\chi^2 = 0.90$, polarization = (0.887 + 0.031 - 0.039))

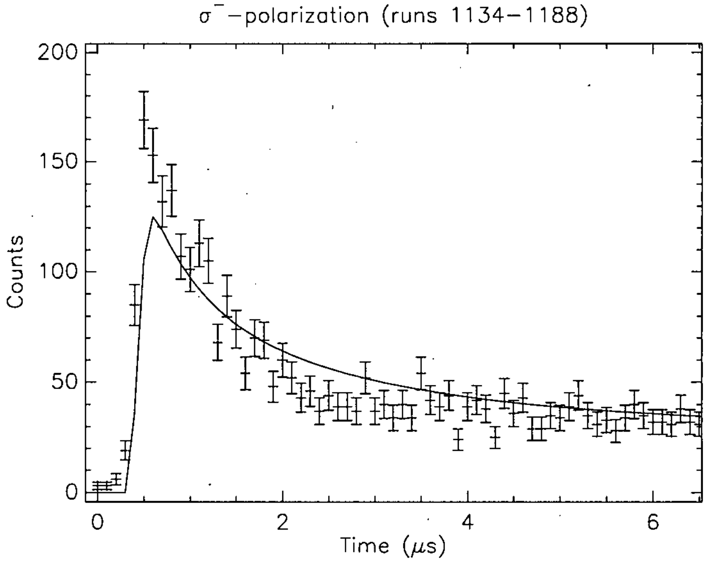

Figure 4.6: Fit to second-week data (σ^+ polarization) (reduced $\chi^2 = 1.1901$, polarization = (0.868 + 0.020 - 0.010))

	σ^-		σ^+	
	+	-	+	-
Statistical	0.031	0.039	0.023	0.011
Total Power	0.010	0.007	0.015	0.021
Power Ratio	0.002		0.002	
Resonance Value	0.014		0.012	
Laser Splitting	0.001		0.001	
Carrier Frequency	0.010		0.009	
On-Axis Magnetic Field	0.010	0.009	0.013	
Total Systematic	0.022	0.021	0.026	0.030

Table 4.2: Summary of errors in atomic polarization measurements

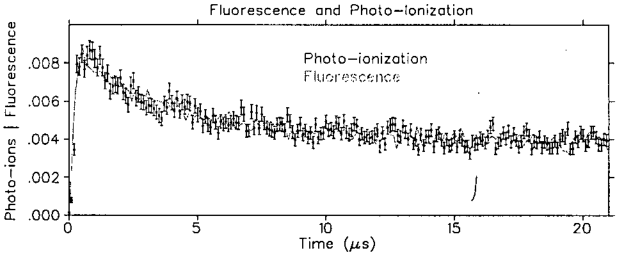

Figure 4.7: Comparison of ^{41}K photoion spectrum with fluorescence spectrum. (from [14])

virtually all of the other parameters determined in Sections 4.2, 4.4, and 4.5 do contribute to the overall error.

The effect of these parameter errors is different for the two polarizations, as the system is highly nonlinear. In addition, several of the larger uncertainties are, like the statistical uncertainties shown in Figures 4.5 and 4.6, asymmetrical. Table 4.2 summarizes the error contribution from each parameter. The systematic errors were added in quadrature as they are essentially independent. Thus, the measurement of polarization from the photoion spectra is $-0.887^{+0.031}_{-0.039}{}^{+0.022}_{-0.021}$ for σ^- light, and $0.868^{+0.020}_{-0.010}{}^{+0.026}_{-0.030}$ for σ^+ light.

There is a possible systematic effect in the photoionization process, in that there could be a dependence of the photoionization cross-section on the m_F value of the atom. Such a dependence could skew the polarization measurement as the simulation calculates the total excited state population unbiased by differences in measurement between the states. After the run of the experiment a cross-check was made between the time dependence of the photoionization rate and the time dependence of the atomic fluorescence during optical pumping with a trap of stable ^{41}K. Both should be proportional to the total excited state population, and thus fitting one to the other will help verify this proportionality. The two observables were found[14] to agree, with a χ^2/ν of 1.7, and the result of the fit can be found in Figure 4.7.

Part II

Nuclear Physics

Chapter 5

Theory of Beta Asymmetries

While the atomic polarization diagnostics must be made using a measurement of the transition from the initial to the final state, nuclear processes can provide a direct measurement of the properties of the final state. A net nuclear polarization can be observed through its production of an asymmetry in the angular distribution of the beta particles. This chapter will discuss the origin of this asymmetry and the means to determine the polarization from the asymmetry. The use of two different methods provides an important cross-check on the polarization measurement.

5.1 Beta Decay Basics

When radioactive decay was discovered by Becquerel near the turn of the century[12], it was soon discovered that the radiation thus produced is split by an electromagnetic field into three components. One component was found to be positively charged, a second negatively charged, and the third electrically neutral; these were labelled alpha, beta, and gamma rays, respectively. Further research determined not only that these components have vastly different properties but also that their origins lie in different nuclear processes.

Beta decay is at its root the transformation of a proton in a nucleus into a neutron, or of a neutron into a proton. To conserve charge, the nucleon emits either an electron, which is the 'beta particle' observed by Becquerel, or a positron. Conservation of lepton number demands the simultaneous emission of a neutrino, which allows the beta particle to take on a spectrum of energy values rather than the monoenergetic emission characteristic of a two-body decay. We can write the processes of beta decay in equation form as

$$n \rightarrow p + e^- + \bar{\nu}_e \tag{5.1}$$

$$p \rightarrow n + e^+ + \nu_e \tag{5.2}$$

The context of the nucleus allows the reaction in Equation 5.2 to proceed despite the increase in rest mass from the initial proton to the particles on the right-hand side.

Beta decay is the dominant decay channel for the majority of light unstable nuclei, and is allowed when the mass difference between the nucleus and one with the same mass

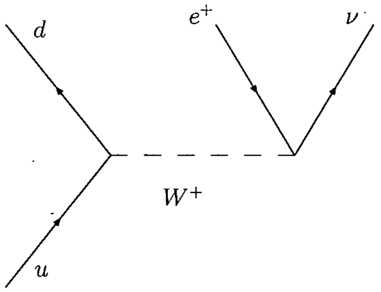

Figure 5.1: Feynman diagram for β^+ decay

number and $\Delta Z = \pm 1$ is larger than the mass of the electron. The minimum mass isotopes for a given mass number thus form a 'valley of stability' in the chart of the nuclides, with the other nuclides transitioning towards the minimum through beta decay.

Beta decay is mediated by the weak nuclear force. The nucleon decays when one of the quarks in the nucleon emits a virtual W boson, which in turn decays, producing an electron and a neutrino. The emission of the W changes the flavour of the quark from up to down (or vice versa), while carrying away one unit of electric charge. The tree-level Feynman diagram for β^+ decay can be found in Figure 5.1. In reality, the quark is not bare, but is instead incorporated in a nucleon with two other quarks. These two other quarks are 'spectator' quarks and do not directly contribute to the beta decay (and are thus not shown), but do interact with the decaying quark through the strong nuclear force.

After emitting a beta particle, the nucleus recoils. This recoil momentum can often be quite large, and appears very quickly compared to atomic timescales. In addition, the charge of the nucleus has changed by one, changing the depth of its Coulomb potential. These changes suddenly shift the electron orbitals in the atom, with the effect that some of the more loosely-bound electrons may fall out of the atomic potential. These 'shake-off' electrons can be detected using the apparatus described in Section 6.2, giving both accurate timing information and background reduction. In the case of ^{80}Rb, the β^+ decay produces a Kr$^-$ ion whose outermost electron is thought to be unbound[9] and thus guaranteed to shake off, and so a shake-off electron should be detected for all decays, notwithstanding detector efficiency .

Another possibility for neutron-deficient isotopes is electron capture, i.e.

$$p + e^- \to n + \nu_e \tag{5.3}$$

This reaction occurs for all β^+ isotopes, but if the energy difference between the initial and final nucleus is less than the electron mass of 511 keV/c^2, electron capture is the only possible decay. Electron capture rates increase with the overlap between the nucleus and

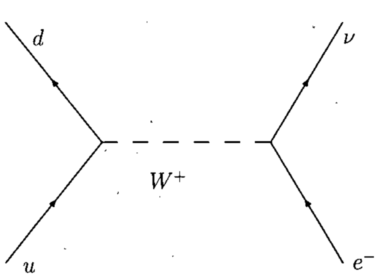

Figure 5.2: Feynman diagram for electron capture

atomic electron wavefunctions, so while it is a relatively small contribution for light elements, heavy elements can have large electron capture branching ratios despite the availability of beta decay. The Feynman diagram for electron capture can be found in Figure 5.2. ^{80}Rb has an electron capture branching ratio of approximately 1%.

The rarest beta decay variant is double beta decay. If we have that $m(Z) < m(Z\pm1)$, but $m(Z) > m(Z\pm2)+2m_e$, the isotope of atomic number Z can decay to the isotope of atomic number $Z\pm2$ via double beta decay. Such a distorted mass spectrum is commonly produced by nucleon pairing. Since double beta decay is a higher-order process than ordinary single beta decay, the rate is much lower.

5.2 Parity Violation

It is usually assumed that any physical interaction will be invariant under parity transformations. If this is true, both the interaction in question and its spatial mirror image are equally physical. Most systems, including all classical systems, are parity invariant, but systems that involve the weak interaction interestingly are not. This was discovered in the late 1950s in experiments led by C.S. Wu[35]. Moreover, this violation is not subtle, but maximal; leptons produced in weak interactions have completely indeterminate parity[22].

In a polarized beta decay experiment like Wu's, the spin polarization direction of the nucleus provides a reference axis from which the decay may be viewed. As spin is an axial vector quantity, the polarization direction is invariant under a parity transformation. Thus, parity invariance would require front-back symmetry of the angular distribution of the beta particles. Instead, the observed angular distribution was strongly forward-peaked, which, since momentum is a vector quantity, means that the parity transformation of the angular distribution would be strongly reverse-peaked with respect to the spin direction of the nucleus. These two situations are clearly distinguishable and thus the physics violates symmetry under parity transformations.

Parity violation is a direct consequence of the $(V-A)$ form of the weak interaction discussed briefly in Section 1.2. The vector and axial vector terms have opposite behaviour under parity transformations, and thus under a parity transformation $(V - A)$ becomes $(V + A)$, ignoring an overall negative sign. Thus, the mixture of couplings with different parity violates parity invariance. The maximality of parity violation in the weak force is due to the two components having equal magnitude. In fact, the original formulation of parity-violating $(V - A)$ interactions had the form $(V + \epsilon A)$, where the discovery of maximal parity violation set $\epsilon = -1$.

Parity violation is the cornerstone of weak interaction physics; all observed parity-violating processes involve the weak interaction and thus it can be used to identify the influence of the weak interaction in a process. In the Standard Model, parity violation is responsible for confining the neutrino and antineutrino to a single helicity each, a statement that is modified only slightly by the existence of neutrino masses. A previous TRINAT experiment[23] searched for evidence of non-Standard Model couplings to 'wrong-handed' neutrinos, and a corresponding slight non-maximality of parity violation in beta decay.

5.3 Relationship with Polarization

In our beta decay experiment, as in Madame Wu's experiment, parity violation's primary observable effect is in the angular distribution of the beta particle, as defined with respect to the nuclear spin direction. In the trap, we have atoms of various spin states, and wish to determine their average direction. Since the angular distribution with respect to the spin direction is well-defined, the overall angular distribution of the beta particles from the trap is thus sensitive to the polarization of the atoms in the trap.

Consider two beta particle detectors situated on the optical pumping axis, one in the forward direction and one in the reverse direction. Neglecting detector backgrounds and resolutions, we would expect that, since the angular distribution is peaked in the forward direction and zero in the reverse direction, if the nuclei in the trap are perfectly polarized, we will only see beta particles in the forward detector. If, instead, the trap is completely unpolarized, the two detectors should observe equal numbers of particles. This is because the nuclear spins are uniformly distributed in direction, and thus there is no preferred axis on which to reference an overall beta distribution.

The interesting case for this work is when the atoms in the trap are *partially* polarized. In this case, the angular distribution will be 'smeared' out in proportion to the degree of polarization. Then, there will still be an asymmetry between the forward and reverse detectors, but it will not be 100%, and this asymmetry will be proportional to the degree of polarization.

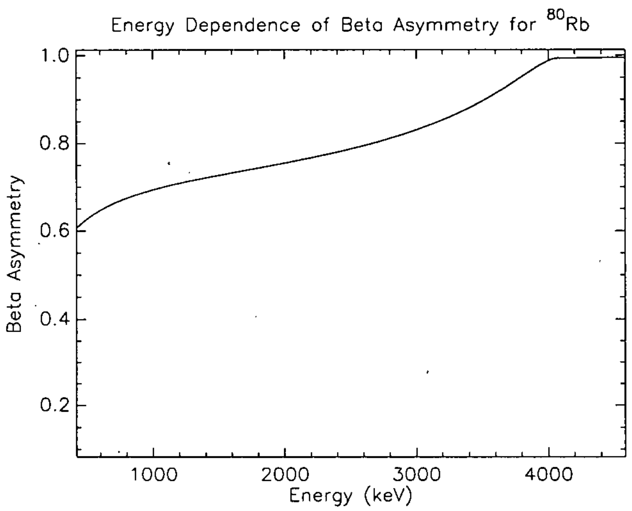

Figure 5.3: Beta asymmetry plot for ^{80}Rb

Specifically, the angular distribution has, in terms of the polarization P, the form[20]

$$W(\theta) = 1 + PA_\beta \cos\theta \tag{5.4}$$

where θ is the angle between the polarization axis and the direction of the beta particle. In the Standard Model, the beta asymmetry A_β for ^{80}Rb's $I = 1 \rightarrow I = 0$ decays is exactly 1, and for the $I = 1 \rightarrow I = 2$ decays it is exactly -1/2[19]. Any correction to this due to the unknown tensor interaction will be small, so for the purpose of determining the polarization it will be neglected. Since the two decays have different endpoints, the fraction of beta particle that derive from one decay or the other varies with energy. In particular, the highest-energy betas are beyond the endpoint of the $I = 1 \rightarrow I = 2$ decay and should have a beta asymmetry of exactly 1. The variation of the asymmetry with energy can be found in Figure 5.3[6].

If the beta spectra are summed over energy, then the beta asymmetries are just scaled by the branching ratios. Since the total branching ratio to $I = 0$ states is 76.3%, and the total branching ratio to $I = 2$ states is 23.7%, we have that the overall beta asymmetry for ^{80}Rb is

$$A_\beta = 1 \times 0.763 - 0.5 \times 0.237 = 0.645 \tag{5.5}$$

Thus, if the beta detectors were along the optical pumping axis then the number of counts in the forward detector would be proportional to $(1+PA_\beta)$, and the number of counts in the reverse detector would be proportional to $(1 - PA_\beta)$. Therefore, their difference is proportional to the polarization P, and the asymmetry $(N_f - N_b)/(N_f + N_b)/A_\beta$ is equal to the polarization. However, the beta detectors in the TRINAT apparatus are actually mounted on an axis inclined by 30 degrees from the optical pumping axis. We have that $\cos(\pi/6) = \sqrt{3}/2$, so the polarization is given by

$$P = \frac{2}{\sqrt{3}} \frac{1}{A_\beta} \frac{N_f - N_b}{N_f + N_b} \tag{5.6}$$

There are small corrections to this equation due to the deviation of the electron velocity from the speed of light, which like the beta asymmetry vary with energy. Since this correction cannot be applied in a summed-up form as in Equation 5.5, the variation of asymmetry with energy will be examined in Section 6.3.

Chapter 6

Beta Detection for Polarization Measurements

6.1 Phoswich Operation

The ‘phoswich’ detectors used to detect the beta particles consist of a thin, fast plastic scintillator bonded to the front of a larger Eu-doped CaF_2 scintillator. The plastic scintillator component is a 2mm thick 1-inch diameter piece of BC408, while the CaF_2 is 20mm long and has a 1.5-inch diameter. The plastic scintillator, being thin, measures the dE/dx of the incident particle, while the CaF_2’s size allows it to measure the total energy E. The intent of the dual-component detector is to distinguish between beta particles and gamma rays, the latter being prevalent in the system due both to gamma emission following beta decay and to positron annihilation. As gamma rays and charged particles interact differently over the thin plastic scintillator, that signal can be used to distinguish between a photon and a positron of the same energy. The plastic scintillator has an energy loss of about 1.8 MeV/cm for beta particles in our energy range, so we expect to see about 360 keV of energy deposited in the thin plastic.

The two scintillators are read out by a single photomultiplier tube, but the difference in timing allows the two signals to easily be separated electronically. The plastic scintillator produces a ‘spike’, which can be measured using a charge-sensitive ADC and serves as a trigger for a peak-sensitive ADC that detects the slower signal from the CaF_2. This is possible because the total width of the plastic scintillator signal is much less than the rise time of the CaF_2.

For simplicity in handling and in electrical connections, the phoswich detectors are situated outside the vacuum system at atmospheric pressure. The drawback to this approach is that the beta particles to be detected must pass out of the vacuum chamber, and thus necessarily through some form of window. The penetrating power of beta particles is limited, so most conventional choices for the window are not feasible. A thin (0.015”) beryllium foil was used as a window for the beta particles to minimize the effect of the window on the beta particles escaping from the vacuum system.

One can plot the data from the phoswiches as a 2D histogram, with the ΔE (fast)

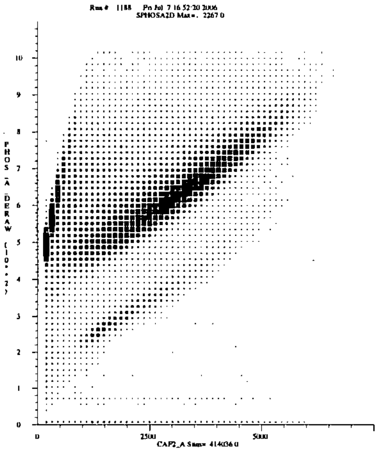

Figure 6.1: 2D histogram of phoswich data

signal along one axis and the total energy (slow) signal along the other axis. In this form, beta particles and gamma rays can be distinguished, appearing in different regions of the histogram. An example phoswich spectrum from ^{80}Rb (in coincidence with a shake-off electron as described in Section 6.2) can be found in Figure 6.1. In this figure, the beta particles fall in the thick diagonal band, and gamma rays fall into a thin streak below the betas. Few gamma rays are present in the spectrum for ^{80}Rb as the gamma ray energies of 616 keV, 1.2 MeV, and 1.3 MeV are smaller than the usual beta energy of 2-3 MeV, they have small branching ratios, and the electronics has an effectively higher threshold due to a short delay in the constant fraction discriminator.

6.2 Electron Detection for Background Control

As described in Section 5.1, an atom undergoing beta decay 'shakes off' one or more electrons as it recoils from the decay. Detection of these electrons in coincidence with the recoiling ion was demonstrated by a group at Berkeley[28], and a similar setup was constructed for the TRINAT ^{80}Rb experiment.

A second micro-channel plate (MCP) was installed at the opposite end of the detection chamber from the original MCP detector. This geometry allows the same static electric field to collect both the shake-off electrons and the (positive) ions onto their respective detectors. Unlike the ion MCP, the MCP for shake-off electron detection is not position sensitive; this is both for simplicity and because the position of the shake-off electrons at the detector is not of kinematic importance.

To maintain the uniformity of the electric field in the chamber, a grid electrode was placed in front of the electron MCP. This is necessary as the potential at the end of the chamber is 5 kV, but restrictions in the power supply and feedthroughs prevent the MCP from being floated to this level. With the grid held at 5 kV, the front of the MCP can be set to any necessary level without significantly perturbing the electric field in the chamber. At the same time, the grid allows electrons to pass unhindered towards the MCP, which will collect the electrons as long as the potential on the front electrode is higher than the potential at the trap position.

This detector also works, though with a different efficiency, as a detector for beta particles. The beta particles are approximately unaffected by the electromagnetic fields that focus the shake-off electrons onto the detector, so only beta particles emitted in the direction of the electron detector can hit it. Nevertheless, this is a significant background for the electron-recoil coincidence. Several runs with the detector voltages adjusted to exclude shake-off electrons from the trap were made to examine this background.

This detector has two main purposes. The first is to provide a time reference to determine the time-of-flight (TOF) of the recoiling ions. The variation in the electron TOF is on the order of a few nanoseconds, much smaller than the microsecond variation of the ion TOF, as the electrons are accelerated more strongly by the electric field, so the time difference between the electron detector hit and the ion MCP hit is a good measure of the ion TOF.

The second purpose, more important for this work, is to control backgrounds in other detectors. Coincidence with an electron detector hit makes it much more likely that a detector hit is the result of beta decay from a trapped atom. This is especially important for the phoswich detectors described above. The background in these detectors is considerable, but the electron detector rejects much of it. While using the raw phoswich signal as an event trigger would overwhelm the data acquisition system with background events, the coïncidence of an electron detector hit and a phoswich hit provides a useful subsidiary event trigger.

Triggering on the electron-phoswich coincidence allowed the collection of data for measuring the asymmetry in the angular distribution of the betas independent of the characteristics of the ion MCP. Given the efficiency and limited solid angle of the MCP, this provides a more accurate sampling of the beta angular distribution.

6.3 Results

In Figure 6.1, the beta particles form a thick diagonal band in the E-ΔE plane. To exclude gamma rays and scattered beta particles, a cut was made that encompassed the beta band. Since the other phoswich has a threshold effect around 1 MeV and sees no counts below that energy, an energy cut was made to restrict the count to the region examined by the two

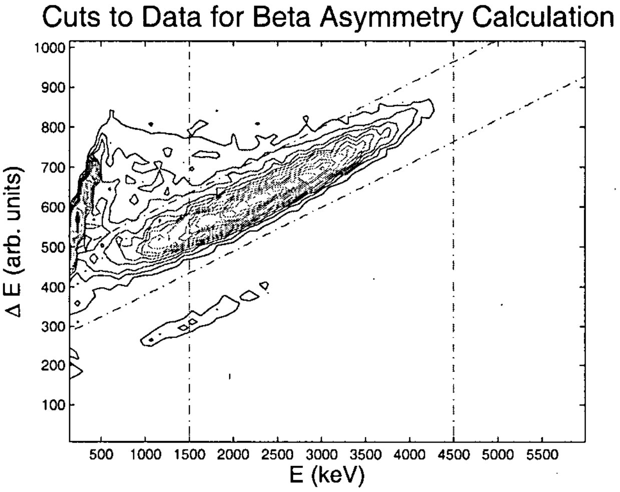

Figure 6.2: Illustration of energy cuts applied for beta asymmetry measurement

detectors. These cut are shown in Figure 6.2. From the data in this region, the polarization for σ^+ was found to be (0.543 ± 0.006), and the polarization for σ^- was found to be (0.617 ± 0.006). The errors on these values are purely derived from counting statistics and do not include any possible systematic effects. These values are inconsistent with the values derived from the atomic physics.

As there exist energy-dependent corrections to the polarization, the polarization should be calculated as a function of energy. Figure 6.3 shows the phoswich data from Figure 6.2 projected onto the energy axis. Once the energy cuts were applied to deal with threshold effects, the data was segmented into 100 keV wide bins, and the asymmetry calculated as per Section 5.3. These values were then corrected by the corresponding value of v/c for a beta particle of that energy, as well as the energy-dependent beta asymmetry as shown in Figure 5.3. The result can be found in Figure 6.4. These graphs are far from linear. The profiles towards the high end are very similar, which suggests a systematic trend favouring one phoswich over the other. This area contains the region with $A_\beta = 1$, preventing the polarization from being read directly off the graph.

Differences in efficiency, gain, and calibration between the two phoswich detectors can act to produce these systematic differences and skew the results obtained from the asymmetries. It is also possible to estimate the polarization from the asymmetry in a single detector between the two polarizations, i.e. $(N_+ - N_-)/(N_+ + N_-)$. Graphs of the polarization as determined from this observable can be found in Figure 6.5. The polarization was determined by fitting a horizontal line to each energy profile. In the case of phoswich A, the polarization was found to be (0.51 ± 0.01), the fit having a χ^2/ν of 3.44. In the case

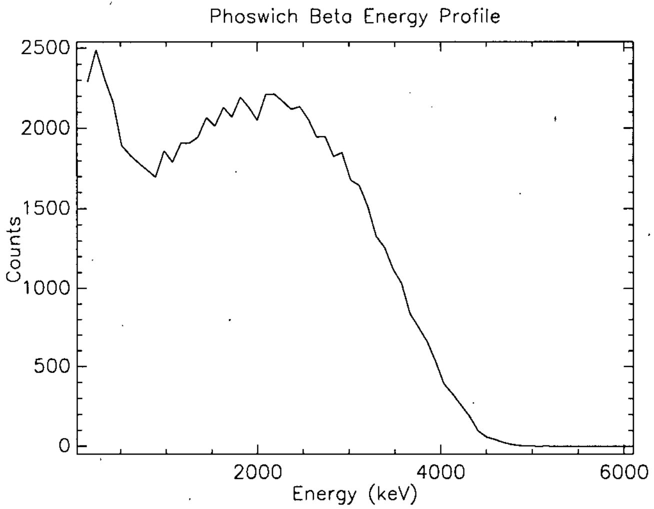

Figure 6.3: Phoswich beta energy spectrum

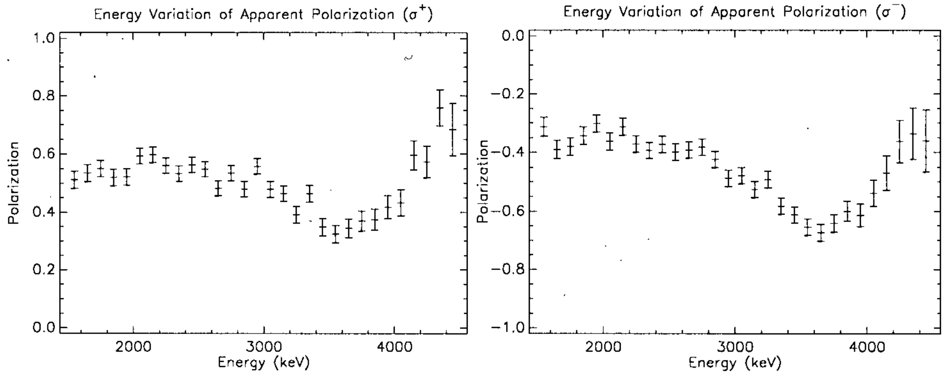

Figure 6.4: Apparent polarization variation with energy

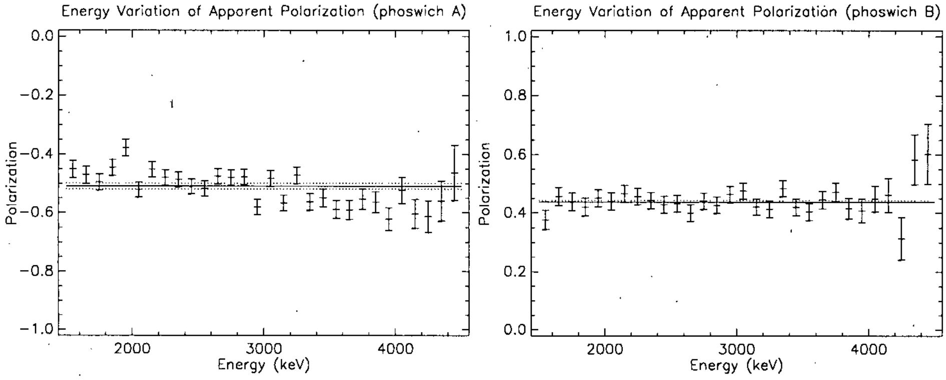

Figure 6.5: Polarization from single-detector asymmetry

of phoswich B, the polarization was (0.44 ± 0.01) with a χ^2/ν of 0.934.

Even with the corrections, the value of polarization derived from the nuclear physics is highly inconsistent with that derived from the atomic physics. This may be the result of unknown systematic problems in beta detection, but could also be related to the approximations of the optical pumping simulation. The simulation makes the crucial assumption that the trap is pointlike and so therefore all sees the same magnetic field and incident laser power. The actual trap is 2–4 mm in diameter, so it is entirely possible that the outer part of the trap would be optically pumped less than the core of the trap. As the nuclear diagnostic is not sensitive to the location of atoms in the trap, these lower-polarization atoms would be measured directly by the nuclear diagnostic. Nevertheless, there remain systematic differences in the polarization measured with the two detectors.

Chapter 7

Conclusion

Polarization diagnostics are important for any spin-polarized experiment. In the case of the ^{80}Rb beta-decay experiment, two independent diagnostic methods were available, one based on the atomic physics of optical pumping, and one based on the nuclear physics of beta decay.

For evaluating the polarization from atomic physics, a simulation based on the rate equations was used. The rate equations were found to be sufficient for the system, rather than requiring the optical Bloch equations. Although the basic rate equations in the $|Fm_F\rangle$ basis were sufficient to include most of the trap conditions, the off-axis magnetic field required the introduction of a more sophisticated technique. The Hamiltonian was calculated for the interaction of the atomic angular momentum and the magnetic field, and then numerically diagonalized to find a new basis to be used in the rate equations. This simulation was compared to the excited state population as measured by photoionization of the excited state during the optical pumping. This photoionization method gives the variation of the excited state population as a function of time over the length of the optical pumping cycle. The background from this method is measurable and was found to be negligible.

The resulting fits to the photoion data from the second week of the experiment give polarizations of $-0.887^{+0.031}_{-0.039}{}^{+0.022}_{-0.021}$ for σ^- light, and $0.868^{+0.020}_{-0.010}{}^{+0.026}_{-0.030}$ for σ^+ light. These values agree with values estimated from a simple, approximate model based on the peak-to-tail ratio of the excited state population graph.

The nuclear diagnostic can be used in two different ways: with an asymmetry between detectors in a given polarization state, or with an asymmetry between polarization states for a given detector. Both of these methods were used in the work, with differing degrees of success. In both cases, energy dependent corrections appear due to relativistic effects and the energy dependence of the beta asymmetry for ^{80}Rb which arises from the different endpoints of branches with different beta asymmetries.

The asymmetry between detectors was found to be sensitive to too many systematic differences between the two detectors, including differing backgrounds, to provide a sensible polarization value. In comparison, the single-detector asymmetries ignore these effects, and as such they provide a much cleaner measurement of the polarization, though they ignore any difference in polarization between the two signs. The energy dependent effects match the theoretical understanding to within the statistical accuracy, giving polarization values of (0.44 ± 0.01) and (0.51 ± 0.01) for the two detectors. These values are grossly inconsistent with the values from the atomic diagnostics.

A possible source of this discrepancy is non-uniformity of the optical pumping over the trap; the atomic diagnostic only measures the component of the trap that is being pumped and in proportion with the amount of pumping, which may vary over the extent of the trap with variations in absorption probability. The absorption probability can vary due to nonuniform in the magnetic field and in the pumping laser power. In contrast, the nuclear detectors view the entire trap, presumably without bias. Additionally, while the nuclear diagnostics measure the polarization averaged over the optical pumping cycle, the atomic diagnostics measure the final polarization attained at the end of the cycle. Furthermore, the uncertainty given for the nuclear diagnostics is purely statistical in nature, with systematic errors and backgrounds remaining unknown and possibly large. Nevertheless, with the discrepancy between the two detectors and a large difference between the two diagnostics, there remain many unanswered questions. Future work of the collaboration will also use polarization diagnostics from ion-beta coincidences, which though they require more elaborate theoretical setup should have substantial polarization sensitivity and low background. Segmenting the spatial extent of the trap and measuring the variation of the apparent polarization with position should help explain the discrepancy, and studies of the polarization with stable ^{41}K should also aid in an understanding of the characteristics of the magnetic field and photoionization laser for future spin-polarized decay experiments.

Bibliography

[1] Nist atomic spectra database, 2005.

[2] E.S. Abers. *Quantum Mechanics.* Pearson Education, 2004.

[3] L. Allen and J.H. Eberly. *Optical Resonance and Two-Level Atoms.* Dover, 1987.

[4] E. Arimondo, M. Inguscio, and P. Violino. Experimental determinations of the hyperfine structure in the alkali atoms. *Rev. Mod. Phys.*, 49(1):31–75, 1977.

[5] A. Ashkin and J Gordon. Stability of radiation-pressure particle traps: an optical earnshaw theorem. *Opt. Lett.*, 8:511–513, 1983.

[6] J.A. Behr. private communication.

[7] D.J. Berkeland and M.G. Boshier. Destabilization of dark states and optical spectroscopy in zeeman-degenerate atomic systems. *Phys. Rev. A*, 65:033413, 2002.

[8] W.E. Boyce and R.C. DiPrima. *Elementary Differential Equations and Boundary Value Problems.* Wiley, seventh edition, 2001.

[9] C.F. Bunge et al. Systematic search of excited states of negative ions lying above the ground state of the neutral atom. *Nucl. Inst. Meth.*, 202:299–305, 1982.

[10] Robert D. Cowan. *The Theory of Atomic Structure and Spectra.* University of California Press, 1981.

[11] D. Das and V. Natarajan. Precise measurement of hyperfine structure in the $5^2p_{1/2}$ state of rb. *Eur. Phys. J. D*, 37:313–317, 2006.

[12] R.D. Evans. *The Atomic Nucleus.* McGraw-Hill, 1955.

[13] C.J. Foot. *Atomic Physics.* Oxford University Press, 2005.

[14] A. Gaudin. private communication.

[15] A. Gorelov et al. Scalar interaction limits from the $\beta - \nu$ correlation of trapped radioactive atoms. *Phys. Rev. Lett.*, 94:142501, 2005.

[16] D. Griffiths. *Introduction to Elementary Particles.* John Wiley & Sons, 1987.

[17] S. Gu, J.A. Behr, M.N. Groves, and D. Dhat. Coherent population trapping states with cold atoms in a magnetic field. *Opt. Comm.*, 220:365–370, 2003.

[18] J.D. Jackson. *Classical Electrodynamics.* John Wiley and Sons, third edition, 1999.

[19] J.D. Jackson, S.B. Treiman, and H.W. Wyld. Coulomb corrections in allowed beta transitions. *Nuc. Phys*, 4:206–212, 1957.

[20] J.D. Jackson, S.B. Treiman, and H.W. Wyld. Possible tests of time reversal invariance in beta decay. *Phys. Rev.*, 106(3):517–521, 1957.

[21] R.L. Liboff. *Introductory Quantum Mechanics.* Addison-Wesley, third edition, 1998.

[22] H.J. Lipkin. *Beta Decay for Pedestrians.* Dover, 2004.

[23] D.G. Melconian. *Measurement of the Neutrino Asymmetry in the Beta Decay of Laser-Cooled, Polarized* ^{37}K. PhD thesis, Simon Fraser University, 2005.

[24] A. Messiah. *Quantum Mechanics*, volume 2. John Wiley & Sons, 1962. Translated by J. Potter.

[25] H.J. Metcalf and P. van der Straten. *Laser Cooling and Trapping.* Springer-Verlag, 1999.

[26] J.R.A. Pitcairn. Master's thesis, University of British Columbia, in preparation.

[27] W.H. Press, B.P. Flannery, S.A. Teukolsky, and W.T. Vetterling. *Numerical Recipes: The Art of Scientific Computing (Fortran version).* Cambridge University Press, first edition, 1989.

[28] N.D. Scielzo et al. Detecting shake-off electron coincidences to measure β-decay correlations in laser-trapped ^{21}na. *Nuc. Phys. A*, 746:677–680, 2004.

[29] J.E. Simsarian, L.A. Orozco, G.D. Sprouse, and W.Z Zhao. Lifetime measurements of the 7p levels of atomic francium. *Phys. Rev. A*, 57(4), 1998.

[30] D. Suter. *The Physics of Laser-Atom Interactions.* Cambridge University Press, 1997.

[31] U. Tanaka and T. Yabuzaki. Simultaneous improvement of short- and long-term frequency stability of a diode laser. In Y.C. Chung, editor, *Frequency-Stabilized Lasers and Their Applications*, volume 1837 of *SPIE Proceedings*, pages 70–80, 1992.

[32] C. Thibault et al. Hyperfine structure and isotope shift of the d_2 line of $^{76--98}$rb and some of their isomers. *Phys. Rev. C*, 23(6):2720–2729, 1981.

[33] S.B. Treiman. Recoil effects in k capture and β decay. *Phys. Rev.*, 110(2):448–450, 1958.

[34] J. Vanier, J.F. Simard, and J.S. Boulanger. Relaxation and frequency shifts in the ground state of rb^{85}. *Phys. Rev. A*, 9:1031–1040, 1974.

[35] C.S. Wu et al. Experimental test of parity conservation in beta decay. *Phys. Rev.*, 105(4):1413–1415, 1957.

Appendix A

Source Code of Simulation

opdr.F:

```
      subroutine OP(spol, p1, d1, p2, d2, Bz, Bx)
      implicit none
************************************************************
* Parameters are as follows:
* spol(-1:1) : Coefficients of the three polarizations
* p1         : Power of F=1/2->F=3/2 beam (in mW/cm^2)
* d1         : Detuning of F=1/2->F=3/2 beam (in MHz)
* p2         : Power of F=3/2->F=3/2 beam (in mW/cm^2)
* d2         : Detuning of F=3/2->F=3/2 beam (in MHz)
* Bz         : B-field along the quantization axis (in G)
* Bx         : Off-axis B-field (in G)
*
* Uses a rate equation formalism and re-diagonalization of
* the Hamiltonian to accomodate the off-axis magnetic field.
************************************************************
      real*8 spol(-1:1), p1, d1, p2, d2, Bz, Bx

      integer Fg, mg, Fe, me, q, mi, k, l, Hg, qg, He, qe, n
      real*8 xFg, xmg, xFe, xme, xq, xmi, xmj, gF
      real*8 mueg(1:3, -3:3, 1:3, -3:3, -1:1)
      real*8 mateg(1:2, 1:4, 1:2, 1:4, -1:1)
      data mueg/1323*0.0/, mateg/192*0.0/

      real*8 poln(1:3, -3:3), Eg(1:3), Ee(1:3)
      real*8 algn(1:3, -3:3)
      data poln/21*0.0/, Eg/3*0.0/, Ee/3*0.0/, algn/21*0.0/

      real*8 npol(1:2, 1:4), Egnd(1:2, 1:4), Eexc(1:2, 1:4)
      real*8 nalg(1:2,1:4)
```

```
      data npol/8*0.0/, Egnd/8*0.0/, Eexc/8*0.0/, nalg/8*0.0/

      real*8 gamma(1:2, 1:4, 1:2, 1:4),
     $     stimfac(1:2, 1:4, 1:2, 1:4)
      data gamma /64*0.0/, stimfac/64*0.0/

      real*8 H32(4,4), H12(2,2), lambda32(4), lambda12(2)
      data H32/16*0.0/, H12/4*0.0/, lambda32/4*0.0/,
     $     lambda12/2*0.0/

      real*8 coeff(1:2, 1:4, -3:3), eigval(1:2, 1:4)
      data coeff/56*0.0/, eigval/8*0.0/

      integer conv32(4), conv12(2), HFconv(2)
      data conv32/3, 1, -1, -3/, conv12/1, -1/, HFConv/1, 3/

      real*8 popg(1:2,1:4), pope(1:2, 1:4)
      data popg/8*0.0/, pope/8*0.0/
      real*8 dpopg(1:2,1:4), dpope(1:2, 1:4)

      real*8 work(136), sum, usum, lorentzf, time
      real*8 polarization, change, alignment
      integer info

      real*8 d1c, d2c, delta1, delta2, patten

************************************************************
* Declare external functions
************************************************************
      real*8 DWIG3J, DWIG6J, DCLEBG
      real*8 gfactor

************************************************************
* Specify physical and mathematical constants
************************************************************
      real*8 muB, pi, h, c
*     muB in Hz/G
```

```
      parameter (muB = 1.3996E6)
      parameter (pi = 3.14159265358979, h = 6.6260755e-34,
     $     c = 2.99792458e+10)

**************************************************************
* Specify all angular momenta
**************************************************************
      real*8 Lg, Le, Jg, Je, S, I, one
      parameter (Lg = 0.0, Le = 1.0, Jg = 0.5, Je = 0.5,
     $     S = 0.5, I = 1.0, one = 1.0)

**************************************************************
* Specify atomic parameters
**************************************************************
      real*8 dg, de, tau, lambda
      parameter (dg = -233.936E6, de = -27.846E6,
     $     tau = 27.64E-9, lambda = 1.0/12579.0)
      real*8 I0
      parameter (I0 = pi*h*c/(3.0*(lambda**3)*tau))

**************************************************************
* Specify timestep and length of simulation
**************************************************************
      real*8 dt, timelength
      integer nsteps
      parameter (dt = 2.5E-9, timelength = 40.0E-6,
     $     nsteps = timelength/dt)

**************************************************************
* Include the output matrices from the inc file
**************************************************************
#include "opdrsub.inc"
      data outtime /outlen*0.0/, outexc /outlen*0.0/,
     $     outgnd /outlen*0.0/, outnpol /outlen*0.0/,
     $     outnalign /outlen*0.0/

**************************************************************
```

```
* First do the pertinent calculations in the original basis
*************************************************************

* mueg is the matrix element between |Fg, mg> and
*  |Fe, me> for light ofpolarization quantum number q
* (Section 2.3.3)
      do Fg = 1,3,2
         xFg = DBLE(Fg)/2.0
         do mg = -Fg,Fg,2
            xmg = DBLE(mg)/2.0
            do Fe = 1,3,2
               xFe = DBLE(Fe)/2.0
               do me = -Fe,Fe,2
                  xme = DBLE(me)/2.0
                  do q = -1,1,1
                     xq = DBLE(q)
                     mueg(Fg,mg,Fe,me,q) =
     $                    (-1.0)**(1+Lg+S+Jg+Je+I-xFg+xFe-xme)
     $                    *sqrt((2*Jg+1)*(2*Je+1)*(2*xFg+1)*
     $                         (2*xFe+1)*(2*Le+1))*
     $                    DWIG6J(Le, Je, S, Jg, Lg, one)*
     $                    DWIG6J(Je, xFe, I, xFg, Jg, one)*
     $                    DWIG3J(xFg, one, xFe, xmg, xq, -xme)
                  end do
               end do
            end do
         end do
      end do

* calculate polarizations of states
* (Section 3.4)
      do Fg = 1,3,2
         xFg = DBLE(Fg)/2.0
         do mg = -Fg,Fg,2
            xmg = DBLE(mg)/2.0
            poln(Fg, mg) = 0.0
            algn(Fg, mg) = 0.0
```

```
            do mi = -1,1,1
               xmi = DBLE(mi)
               xmj = xmg - xmi
               poln(Fg, mg) = poln(Fg, mg) +
     $           xmi*(DCLEBG(I, Jg, xFg, xmi, xmj, xmg))**2
               algn(Fg, mg) = algn(Fg, mg) +
     $           xmi**2*(DCLEBG(I, Jg, xFg, xmi, xmj, xmg))**2
            end do
            if (abs(poln(Fg, mg)).lt.1E-10) then
               poln(Fg, mg) = 0.0
            end if
            if (abs(algn(Fg, mg)).lt.1E-10) then
               algn(Fg, mg) = 0.0
            end if
         end do
      end do

* energies all referenced against unshifted F=3/2 state
      Eg(1) = -dg
      Ee(1) = -de

**************************************************************
* Now calculate out the new basis (Section 3.2)
**************************************************************

* Diagonal elements of Hamiltonians
      H32(1,1) = muB*Bz*1.5
      H32(2,2) = muB*Bz*0.5
      H32(3,3) = muB*Bz*-0.5
      H32(4,4) = muB*Bz*-1.5

      H12(1,1) = muB*Bz*0.5
      H12(2,2) = muB*Bz*-0.5
* Off-diagonal elements of Hamiltonians (only upper triangle)
      H32(1,2) = muB*Bx*sqrt(0.75)
      H32(2,3) = muB*Bx
      H32(3,4) = muB*Bx*sqrt(0.75)
```

```
      H12(1,2) = muB*Bx*0.5

* now do the eigensolves
      call DSYEV('V', 'U', 4, H32, 4, lambda32, work, 136,
     $     info)
      if (info.ne.0) then
         print *, 'eigensolve broke down, giving up!'
         stop
      end if

      call DSYEV('V', 'U', 2, H12, 2, lambda12, work, 68,
     $     info)
      if (info.ne.0) then
         print *, 'eigensolve broke down, giving up!'
         stop
      end if

* and reorganize the eigenvectors into coefficients
      do k = 1, 4
         do l = 1, 4
            mg = conv32(k)
            coeff(2, l, mg) = H32(k, l)
         end do
         eigval(2, k) = lambda32(k)
      end do
      do k = 1, 2
         do l = 1, 2
            mg = conv12(k)
            coeff(1, l, mg) = H12(k, l)
         end do
         eigval(1, k) = lambda12(k)
      end do

*****************************************************************
* Calculate the matrix elements and expectation values
* in the new basis
```

```
**************************************************************

* do matrix elements first
* (Section 3.3.2)
      do Hg = 1,2,1
         Fg = HFconv(Hg)
         do qg = 1,2*Hg,1
            do He = 1,2,1
               Fe = HFconv(He)
               do qe = 1,2*He,1
                  do q = -1,1,1
                     sum = 0.0
                     do mg = -Fg,Fg,2
                        do me = -Fe,Fe,2
                           sum = sum +
     $                          coeff(Hg, qg, mg)*
     $                          coeff(He, qe, me)*
     $                          mueg(Fg, mg, Fe, me, q)
                        end do
                     end do
                     mateg(Hg,qg,He,qe,q) = sum
                  end do
               end do
            end do
         end do
      end do

* calculate polarization and alignment
* (Section 3.4)
      do Hg = 1,2,1
         Fg = HFconv(Hg)
         do qg = 1,2*Hg,1
            sum = 0.0
            usum = 0.0
            do mg = -Fg,Fg,1
               sum = sum + poln(Fg, mg)*coeff(Hg, qg, mg)**2
               usum = usum + algn(Fg, mg)*coeff(Hg, qg, mg)**2
```

```
              end do
              npol(Hg, qg) = sum
              nalg(Hg, qg) = usum
           end do
        end do

*   calculate energies of states
*   (Section 3.3.1)
        do Hg = 1,2,1
           Fg = HFconv(Hg)
           gF = gfactor(DBLE(Fg)/2.0, Jg, I, S, Lg)
           do qg = 1,2*Hg,1
              Egnd(Hg, qg) = Eg(Fg) + gF*eigval(Hg, qg)
           end do
        end do

        do He = 1,2,1
           Fe = HFconv(He)
           gF = gfactor(DBLE(Fe)/2.0, Je, I, S, Le)
           do qe = 1,2*He,1
              Eexc(He, qe) = Ee(Fe) + gF*eigval(He, qe)
           end do
        end do

*****************************************************************
*   Now calculate the rates in the new basis
*****************************************************************

*   reference to the same place as everything else
        d1c = d1*1E6 + dg
        d2c = d2*1E6

*   rate calculations are Sections 2.3.3 and 2.3.4
        do Hg = 1,2,1
           do qg = 1,2*Hg,1
              do He = 1,2,1
                 do qe = 1,2*He,1
```

```
                 sum = 0.0
                 usum = 0.0
                 do q = -1,1,1
                    sum = sum + spol(q)*mateg(Hg,qg,He,qe,q)
                    usum = usum + mateg(Hg,qg,He,qe,q)**2
                 end do
                 gamma(Hg,qg,He,qe) = usum/tau

                 delta1 = d1c - Eexc(He,qe) + Egnd(Hg,qg)
                 delta2 = d2c - Eexc(He,qe) + Egnd(Hg,qg)
                 lorentzf = p1*1E-3/(I0*2.0*
     $                (1.0+4.0*(2.0*pi*tau*delta1)**2))
     $                   + p2*1E-3/(I0*2.0*
     $                (1.0+4.0*(2.0*pi*tau*delta2)**2))
                 stimfac(Hg,qg,He,qe) = lorentzf*sum**2/tau
              end do
           end do
        end do
     end do

**************************************************************
* and initialize the populations
**************************************************************

     do Hg = 1,2,1
        do qg = 1,2*Hg,1
           popg(Hg, qg) = 1.0/6.0
        end do
     end do

     do He = 1,2,1
        do qe = 1,2*He,1
           pope(He, qe) = 0.0
        end do
     end do

**************************************************************
```

```
* Now loop over all timesteps
*****************************************************************
      time = 0.0
      k = 0
      do n = 1,nsteps
         time = time + dt

*****************************************************************
* Rezero all of our changes
*****************************************************************
         do Hg = 1,2,1
            do qg = 1,2*Hg,1
               dpopg(Hg, qg) = 0.0
            end do
         end do

         do He = 1,2,1
            do qe = 1,2*He,1
               dpope(He, qe) = 0.0
            end do
         end do

*****************************************************************
* Shape the power (Section 3.3.3)
*****************************************************************
         patten = 1.0/(1.0+9.025*EXP(-time/38.5E-9))

*****************************************************************
* Calculate the changes
*****************************************************************
         do Hg = 1,2,1
            do qg = 1,2*Hg,1
               do He = 1,2,1
                  do qe = 1,2*He,1
*           This is the change 'upward' into the excited state
                     change = (patten*stimfac(Hg,qg,He,qe)*
     $                    (popg(Hg,qg) - pope(He,qe)) -
```

```
     $                                    gamma(Hg,qg,He,qe)*
     $                                    pope(He,qe))*dt
                          dpope(He,qe) = dpope(He,qe) + change
                          dpopg(Hg,qg) = dpopg(Hg,qg) - change
                       end do
                    end do
                 end do
              end do

**************************************************************
* Execute the changes
**************************************************************
              do Hg = 1,2,1
                 do qg = 1,2*Hg,1
                    popg(Hg, qg) = popg(Hg, qg) + dpopg(Hg,qg)
                 end do
              end do

              do He = 1,2,1
                 do qe = 1,2*He,1
                    pope(He, qe) = pope(He, qe) + dpope(He,qe)
                 end do
              end do

**************************************************************
* Write out on every fourth timestep
**************************************************************
              if (mod(n, 4).eq.0) then
                 k = k + 1
                 outtime(k) = time

                 sum = 0.0
                 polarization = 0.0
                 alignment = 0.0
                 do Hg = 1,2,1
                    do qg = 1,2*Hg,1
                       sum = sum + popg(Hg, qg)
```

```
               polarization = polarization +
     $                npol(Hg, qg)*popg(Hg,qg)
               alignment = alignment +
     $                nalg(Hg, qg)*popg(Hg, qg)
            end do
         end do
         outgnd(k) = sum

         sum = 0.0
         do He = 1,2,1
            do qe = 1,2*He,1
               sum = sum + pope(He, qe)
               polarization = polarization +
     $                npol(He, qe)*pope(He,qe)
               alignment = alignment +
     $                nalg(He, qe)*pope(He, qe)
            end do
         end do
         outexc(k) = sum
         outnpol(k) = polarization/I
         outnalign(k) = (I*(I+1)-3.0*alignment)/(I*(2*I-1))
      end if
   end do
   npoints = k
   end subroutine OP
***************************************************************
   real*8 function gfactor(F, J, I, S, L)
***************************************************************
* Calculates the g-factor for a given F-state. (Section 3.3.1)
***************************************************************
   implicit none

   real*8 F, J, I, S, L

   real*8 gJ, gF

   if (F > 0.0) then
```

```
         gJ = 1.0 + (J*(J+1.0) + S*(S+1.0) - L*(L+1.0))/
     $           (2.0*J*(J+1.0))
         gF = gJ*(F*(F+1.0) + J*(J+1.0) - I*(I+1.0))/
     $           (2.0*F*(F+1.0))
      else
         gF = 0.0
      end if

      gfactor = gF

      end function gfactor
```

opdrsub.inc:

```
      integer outlen
      parameter (outlen = 4000)

      integer npoints

      real*8 outtime(outlen), outexc(outlen), outgnd(outlen),
     $     outnpol(outlen), outnalign(outlen)

      common /OPOUT/ outtime, outexc, outgnd, outnpol,
     $     outnalign, npoints
```